Phase Equilibria of Pantelleria Trachytes (Italy): Constraints on Pre-eruptive Conditions and on the Metaluminous to Peralkaline Transition in Silicic Magmas

Pierangelo Romano, Joan Andújar, Bruno Scaillet, Nunzia Romengo, Ida Di Carlo, Silvio Rotolo

JOURNAL OF PETROLOGY

Journal of Petrology, 2018, Vol. 59, No. 3, 559–588
doi: 10.1093/petrology/egy037
Advance Access Publication Date: 10 April 2018
Original Article

OXFORD

Phase Equilibria of Pantelleria Trachytes (Italy): Constraints on Pre-eruptive Conditions and on the Metaluminous to Peralkaline Transition in Silicic Magmas

Pierangelo Romano[1]*, Joan Andújar[2,3,4], Bruno Scaillet[2,3,4], Nunzia Romengo[1], Ida di Carlo[2,3,4] and Silvio G. Rotolo[1,5]

[1]Dipartimento di Scienze della Terra e del Mare (DiSTeM), Via Archirafi, Università degli Studi di Palermo, Palermo 36-90123, Italy; [2]Université d'Orléans, ISTO, UMR 7327, 45071 Orléans, France; [3]CNRS/INSU, ISTO, UMR 7327, 45071 Orléans, France; [4]BRGM, ISTO, UMR 7327, BP 36009, 45060 Orléans, France; [5]Istituto Nazionale di Geofisica e Vulcanologia, Sezione di Palermo, Via Ugo La Malfa 153, Palermo 90146, Italy

*Corresponding author. E-mail: pierangelo.romano@unipa.it

Received October 1, 2016; Accepted March 22, 2018

ABSTRACT

The relationships between trachytes and peralkaline rhyolites (i.e. pantellerites and comendites), which occur in many continental rift systems, oceanic islands and continental intraplate settings, is unclear. To fill this gap, we have performed phase equilibrium experiments on two representative metaluminous trachytes from Pantelleria to determine both their pre-eruptive equilibration conditions (pressure, temperature, H_2O content and redox state) and liquid lines of descent. Experiments were performed in the temperature range 750–950°C, pressure 0·5–1·5 kbar and fluid saturation conditions with XH_2O [$= H_2O/(H_2O + CO_2)$] ranging between zero and unity. Redox conditions were fixed below the nickel–nickel oxide buffer (NNO). The results show that at 950°C and melt water contents (H_2O_{melt}) close to saturation, trachytes are at liquidus conditions at all pressures. Clinopyroxene is the liquidus phase, being followed by iron-rich olivine and alkali feldspar. Comparison of experimental and natural phases (abundances and compositions) yields the following pre-eruptive conditions: $P = 1 \pm 0{\cdot}5$ kbar, $T = 925 \pm 25$°C, $H_2O_{melt} = 2 \pm 1$ wt %, and fO_2 between NNO − 0·5 and NNO − 2. A decrease in temperature from 950°C to 750°C, as well as of H_2O_{melt}, promotes a massive crystallization of alkali feldspar to over 80 wt %. Iron-bearing minerals show gradual iron enrichment when T and fO_2 decrease, trending towards the compositions of the phenocrysts of natural pantellerites. Despite the metaluminous character of the bulk-rock compositions, residual glasses obtained after 80 wt % crystallization evolve toward comenditic compositions, owing to profuse alkali feldspar crystallization, which decreases the Al_2O_3 of the melt, leading to a consequent increase in the peralkalinity index [PI = molar $(Na_2O + K_2O)/Al_2O_3$]. This is the first experimental demonstration that peralkaline felsic derivatives can be produced by low-pressure fractional crystallization of metaluminous mafic magmas. Our results show that the pantelleritic magmas of basalt–trachyte–rhyolite igneous suites require at least 95 wt % of parental basalt crystallization, consistent with trace element evidence. Redox conditions, through their effect on Fe–Ti oxide stabilities, control the final iron content of the evolving melt.

Key words: peralkaline silicic magmatism; experimental petrology; trachyte; pantellerite; liquid line of descent; Pantelleria; metaluminous–peralkaline transition

INTRODUCTION

Pantelleria is the type locality of pantellerite, an iron- and alkali-rich rhyolite (peralkalinity index, PI >1·2). Peralkaline rhyolites (i.e. pantellerite and comendite) and trachytes usually represent the felsic end-members in the following settings: (1) continental rift systems (e.g. Pantelleria, Tibesti, Ethiopia, Afar, Kenya, Basin and Range province, South Greenland; Barberi *et al.*, 1975; Civetta *et al.*, 1998; Peccerillo *et al.*, 2003); (2) oceanic island settings (e.g. Socorro, Easter Is., Iceland and the Azores; Macdonald *et al.*, 1990; Mungall & Martin, 1995; Bohrson & Reid, 1997); (3) continental intraplate suites (Liu *et al.*, 1998; Brenna *et al.*, 2015). The origin of peralkaline rhyolites in these different tectonic settings is still a matter of debate and three hypotheses have been suggested: (1) crystal fractionation of alkali basalt magma in a shallow reservoir to produce a trachyte whose subsequent crystallization gives rise to a pantellerite (e.g. Barberi *et al.*, 1975; Mungall & Martin, 1995; Civetta *et al.*, 1998); (2) partial melting of cumulate gabbros to form a trachyte, which then produces pantellerite (e.g. Lowenstern & Mahood, 1991; Bohrson & Reid, 1997); (3) partial melting of different lithospheric sources fluxed by volatiles, which add excess alkalis to the melt (Bailey & Macdonald, 1975, 1987). Recent petrological work has helped to define the temperature range and redox conditions of comenditic to pantelleritic magmas (Scaillet & Macdonald, 2001, 2003, 2006; White *et al.*, 2005, 2009; Di Carlo *et al.*, 2010) as well as their pre-eruptive volatile contents (e.g. Gioncada & Landi, 2010; Neave *et al.*, 2012; Lanzo *et al.*, 2013). In contrast, little is known about the conditions of magma storage and evolution of the associated trachytes. At Pantelleria, trachytes and pantellerites constitute most of the outcropping rocks (e.g. Mahood & Hildreth, 1986), the former being erupted dominantly as lava flows whereas the pantellerites are erupted either explosively or effusively.

We have experimentally investigated the phase relationships of two representative trachytes from Pantelleria to shed light on their pre-eruptive magma storage conditions (pressure, temperature, H_2O_{melt}, oxygen fugacity) and define their liquid lines of descent. We have established the phase relationships at $P = 0{\cdot}5$–$1{\cdot}5$ kbar, $T = 750$–$950^{\circ}C$, $fO_2 \sim NNO - 1$ (where NNO is the nickel–nickel oxide buffer) and XH_2O_{fluid} [$H_2O/(H_2O + CO_2)$, in moles] between unity and zero. By comparing the experimental phase assemblages, abundances and compositions with the natural products we set constraints on the storage conditions of trachytic magmas at Pantelleria and on the putative parent–daughter relationship between trachytic and pantelleritic magmas. Our results form the basis for understanding the long-debated petrological issue regarding the link between silica-oversaturated peralkaline and metaluminous magmas.

GEOLOGICAL SETTING

Eruptive history

The island of Pantelleria is the emerged portion of a large Quaternary volcanic edifice rising from the Sicily Channel rift zone (Fig. 1; Rotolo *et al.*, 2006; Catalano *et al.*, 2009). The eruptive products of Pantelleria form a bimodal suite that consists of mafic (mildly alkali basalt) and felsic (metaluminous or slightly peralkaline trachytes and pantellerites) end-members (Civetta *et al.*, 1998; Avanzinelli *et al.*, 2004; Ferla & Meli, 2006). From the volcanological point of view, the eruptive history of Pantelleria is characterized by large explosive ignimbritic eruptions, low-energy Strombolian eruptions and lava flows. The eruptive history can be divided into three major periods. During the first period (324–180 ka) pantelleritic lavas were mostly erupted, producing either welded tuffs or pumice fallout deposits (Mahood & Hildreth, 1986; Civetta *et al.*, 1988; Rotolo *et al.*, 2013). The second period (180–45 ka) was characterized by more than eight ignimbrite-forming eruptions, including the La Vecchia caldera-forming eruption and the Green Tuff eruption (GT). The GT eruption, recently dated at $44{\cdot}1 \pm 0{\cdot}6$ ka (Scaillet *et al.*, 2013), is the last highly energetic eruption and the only one that blanketed the entire island; about 7 km^3 dense rock equivalent (DRE) of tephra were erupted. Moreover, it is thought to be the cause of the Cinque Denti Caldera, which is nested within the La Vecchia caldera collapse (Fig. 1) (Mahood & Hildreth, 1986; Speranza *et al.*, 2012). During the third period (45–8 ka), the activity consisted of felsic resurgent volcanism confined almost entirely inside the Cinque Denti caldera. This third period started with a long phase of effusive activity that produced at least $\sim$3 km^3 of trachytic lavas, building the Montagna Grande–Monte Gibele system, a large volcanic complex that is tectonically uplifted and tilted and forms the island's highest elevation. This phase was followed by low-energy Strombolian eruptions associated with effusive events, yielding pumice fall sequences, lava flows and lava domes with pantelleritic compositions (Mahood & Hildreth, 1986; Civetta *et al.*, 1998; Rotolo *et al.*, 2007). At the end of the third period, extracaldera basaltic volcanism occurred in the NW side of the island (Fig. 1), simultaneously with pantelleritic magmatism. The last eruptive episode (1891) occurred offshore, at about 5 km off the NW coast, emitting lavas of broadly basaltic composition (Kelly *et al.*, 2014).

Petrological background: the origin of pantellerites and previous constraints on storage conditions

Pantelleria is very well known in the petrological literature for the presence of a typical compositional gap (Daly Gap) in the eruptive sequence between the mafic and felsic end-members. Intermediate products are, however, sporadically found as enclaves within the

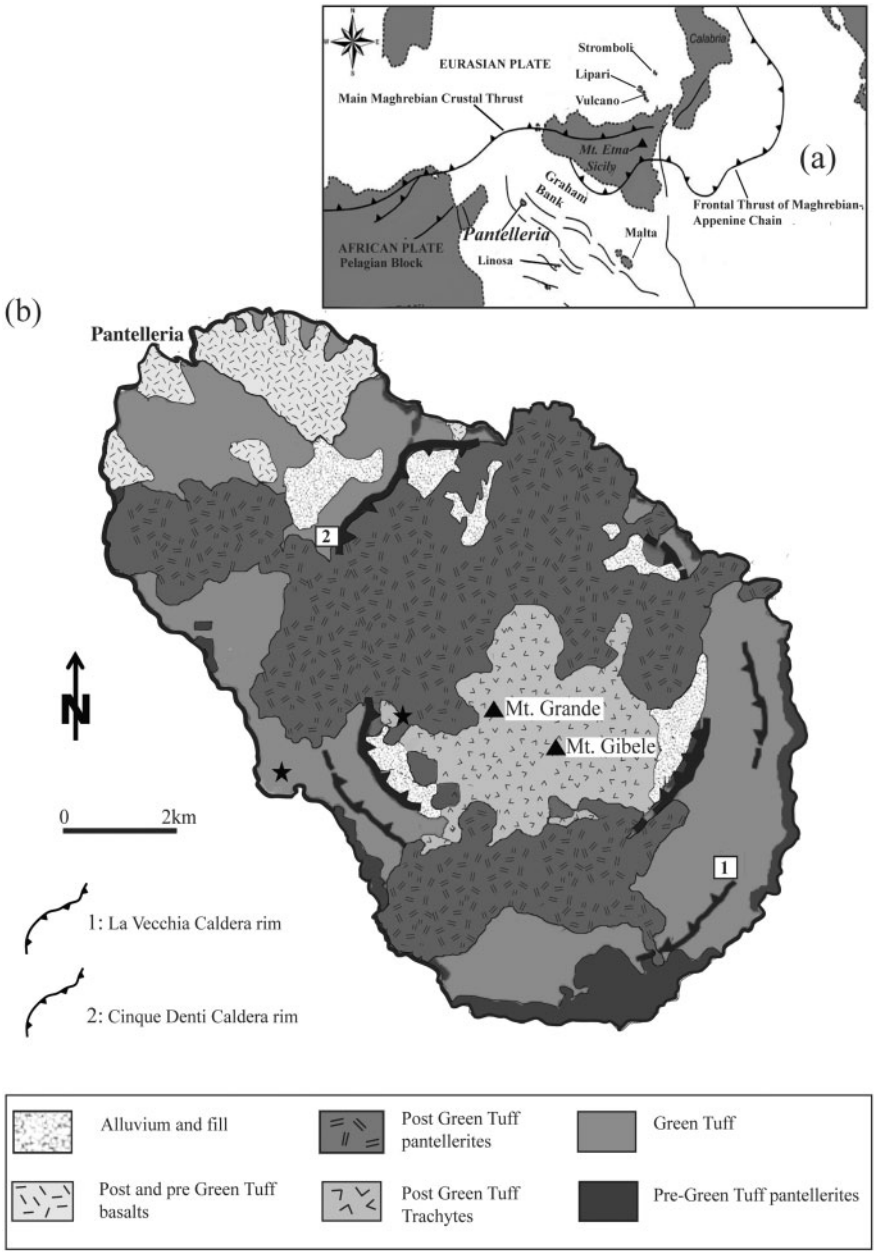

Fig. 1. (a) Tectonic sketch of the Sicily Channel rift zone (modified from Catalano *et al.*, 2009) showing the location of Pantelleria and other volcanic islands (Graham Bank, Linosa) in the rift zone between Sicily and Tunisia. (b) Simplified geological map of Pantelleria; the stars mark the sampling sites of the starting materials used in the experiments.

felsic rocks and as a single small-volume lava flow with a benmoreitic bulk-rock composition. In both cases, these rocks show the characteristics of a magma that originated from basalt–rhyolite mixing (Ferla & Meli, 2006; Romengo *et al.*, 2012).

At Pantelleria, the petrogenesis of pantelleritic rocks has been explained through two models: (1) protracted fractional crystallization from an alkali basalt parental magma; (2) low-degree partial melting of alkali gabbroic cumulates. The first model argues for the fractional crystallization of a mineral assemblage of plagioclase, clinopyroxene, olivine ± Fe–Ti-oxides at an oxygen fugacity around FMQ − 1 (where FMQ is the fayalite–magnetite–quartz buffer), which produced a metaluminous trachytic residual liquid, which then crystallized (∼90%) to yield a pantelleritic magma (Civetta *et al.*, 1998; White *et al.*, 2009; Neave *et al.*, 2012). Alternatively, on the basis of the low water contents observed in melt inclusions of pantelleritic composition, Lowenstern & Mahood (1991) proposed the partial melting of gabbroic cumulates as the source of the trachytic magmas, which then produced pantellerites by low-pressure fractional crystallization. Regarding the pre-eruptive conditions of the mafic suite, Civetta *et al.*

(1998) reported Fe–Ti oxide temperatures in the range 940–1079°C. These values are similar to the 1091 ± 45°C obtained by Neave *et al.* (2012) based on mineral–liquid equilibria. For metaluminous trachytes, based on mineral–mineral or mineral–liquid equilibria, White *et al.* (2005, 2009) reported a temperature range of 858–922°C, whereas for pantellerites they reported a range of 650–750°C. Estimates of redox conditions for Pantelleria magmas yield an fO_2 of around NNO − 1. Such T–fO_2 conditions for pantelleritic melts have been corroborated by phase equilibrium experiments by Di Carlo *et al.* (2010), which in addition demonstrate the water-rich character (up to 4 wt %) of these magmas. Water contents of mafic to felsic melt inclusions (MI) have been also investigated through Fourier transform infrared spectroscopy (FTIR) and secondary ion mass spectrometry (SIMS). Melt inclusions trapped in phenocrysts of alkali basalts yield water contents (H_2O melt) ranging from 0·8 to 1·6 wt % and CO_2 up to 980 ppm (Gioncada & Landi, 2010). Water contents in MI within phenocrysts of pantelleritic magmas vary between 2 and 4·5 wt % (Lowenstern & Mahood, 1991; Gioncada & Landi, 2010; Neave *et al.*, 2012; Lanzo *et al.*, 2013). The corresponding pressures of volatile saturation are <2 kbar, being consistent with both experimental (Di Carlo *et al.*, 2010) and geophysical (Mattia *et al.*, 2007) constraints, altogether suggesting the existence of a shallow magma reservoir at a depth of ∼4 km (1 kbar for an average crustal density of 2·6 g cm^{-3}).

ROCKS STUDIED AND CHOICE OF THE EXPERIMENTAL CONDITIONS

Despite being less abundant than pantellerite, trachytic magmas were erupted during the entire volcanological history of Pantelleria as lava flows (Civetta *et al.*, 1998; White *et al.*, 2009; Romengo, 2011), ignimbrite units (Mahood *et al.*, 1986; Rotolo *et al.*, 2013) and magmatic enclaves (Prosperini *et al.*, 2000; Landi & Rotolo, 2015). We have performed phase equilibrium experiments on two trachytic samples representative of the trachytic rocks at Pantelleria, which are spatially and temporally related to pantelleritic eruptions. On the basis of their petrographic characteristics and major and trace element compositions, these two trachytes were selected because they do not display evidence of feldspar accumulation, unlike most Pantelleria trachytes (Prosperini *et al.*, 2000; White *et al.*, 2009): hence they are likely to be on the relevant liquid line of descent of the studied system. One of the samples (GTT for Green Tuff Trachyte) comes from the trachytic (top-) member of the Green Tuff (GT) formation (36°49′10·90"N, 11°59′49·71"E), whereas the other belongs to one of the post-GT lava flows filling the Cinque Denti caldera (36°46′46·72"N, 11°58′47·23"E), here named PCD (for Post Cinque Denti caldera). The Green Tuff formation, apart from an initial pumice fallout, is considered to be a single pyroclastic flow unit [for details see Williams (2010)]. It displays continuous chemical zoning from pantellerite at the bottom to comenditic trachyte at the top, suggesting a zoned reservoir (Mahood & Hildreth, 1986; Civetta *et al.*, 1998; Williams, 2010). In contrast, the trachytes of M Grande/Gibele (used as starting material, PCD), which erupted immediately after the Cinque Denti caldera collapse, constitute a broadly homogeneous body, with minor differences in major and trace element composition between units, albeit forming a complex system of lava flows (White *et al.*, 2009; Romengo, 2011). According to Mahood & Hildreth (1986), the GT and PCD trachytes are genetically linked, the latter representing the deeper part of a zoned reservoir whose pantelleritic fraction had been removed during the Green Tuff eruption. This large volume of trachyte follows the Green Tuff eruption but also precedes the last explosive post-caldera pantelleritic eruptions (Scaillet *et al.*, 2011).

Bulk-rock compositions of both rocks were obtained by X-ray fluorescence (XRF) and inductively coupled plasma atomic emission spectrometry (ICP-AES) analysis (Table 1), the two rocks falling in the trachytic field of the total alkalis–silica (TAS) diagram (Le Bas *et al.*, 1986). The mineralogy was determined by both petrographic observation and scanning electron microscopy (SEM), and the compositions of mineral phases were determined by electron microprobe analysis (EPMA) (Table 1). The two trachytes have a PI of 1·06 (GTT) and 0·97 (PCD). Crystal contents, based on point counting in thin sections, are ∼34 vol. % for GTT and ∼37 vol. % for PCD. Large alkali feldspars (Af) (0·6 cm) make up ∼32 vol. % of the phenocryst content in GTT and 34 vol. % in PCD. Clinopyroxene (Cpx) and olivine (Ol) have dimensions ranging from 250 to 500 μm, representing 1·5 and 2·8 vol. %, respectively, of the crystal content. The occurrence of large glomerophenocrysts of Af and mafic minerals suggests that Ol and Cpx co-precipitated along with Af. Microphenocrysts of Ti-magnetite (Mt) and ilmenite (Ilm) occur in GTT, either in the groundmass or in glomerophenocrysts (with Af and Cpx), but also within Cpx and Ol. In GTT, Fe–Ti oxides are either homogeneous or display oxy-exsolution textures with intergrowing lamellae of Il in Mt, whereas in PCD all oxides exhibit oxy-exsolution textures. As for oxides, apatite (Ap) crystals are often included in Ol and Cpx. The groundmass in both samples consists predominantly of Af microlites (<0·05 mm), Cpx, oxides and traces of Ol, but PCD also includes traces of quartz (Qz) and amphibole (Amph). A few pockets of residual glass (Gl) were found only in the sample GTT, which is probably due to the different cooling rate between ignimbrite deposits (GTT) and lava flows (PCD). The scarcity of quenched glass in trachytes, also reported by Gioncada & Landi (2010), explains the lack of volatile data for trachytic magmas. Af phenocrysts display compositions ranging from $An_{01–09}Ab_{64–74}Or_{16–34}$ (GTT) to $An_{03–10}Ab_{65–69}Or_{22–29}$ (PCD). Cpx in both rocks is augite ($En_{26–28}$–$Fs_{27–29}$–$Wo_{42–44}$) with XFe [= Fe/(Fe + Mg), calculated using FeO_{tot}] of 0·52 in GTT and 0·49 in PCD,

Table 1: Major element composition of natural Green Tuff (GTT) and Post Cinque Denti Caldera (PCD) trachytes: bulk rock (XRF), mineral phases (EMP) and starting materials (glasses, EMP)

	GTT Bulk-rock	Starting material	SD	Cpx	SD	Ol	SD	Afs pheno	SD	Afs microlite	SD	Mt	SD	Ilm	SD
n:		20		10		4		20		12		3		3	
SiO_2 (wt %)	63·40	64·12	0·39	50·02	0·50	31·72	0·12	65·46	0·54	66·68	0·54	0·06	0·00	0·00	0·01
TiO_2	0·87	0·85	0·09	0·56	0·15	0·00	0·00	0·00	0·00	0·00	0·00	24·62	0·76	49·72	0·59
Al_2O_3	15·15	15·04	0·14	0·60	0·08	0·00	0·00	19·57	0·36	18·57	0·22	0·62	0·13	0·15	0·13
FeO_{tot}	7·10	6·27	0·23	16·96	0·53	52·42	1·84	0·24	0·09	0·79	0·20	66·05	2·58	44·09	0·25
MnO	0·23	0·27	0·08	1·03	0·13	2·84	0·13	0·00	0·00	0·00	0·00	1·59	0·11	1·88	0·45
MgO	0·60	0·62	0·04	9·41	0·22	10·75	0·07	0·00	0·00	0·00	0·00	0·80	0·53	1·02	0·88
CaO	1·29	1·48	0·05	20·12	0·19	0·47	0·01	0·95	0·06	0·56	0·09	0·01	0·01	0·05	0·01
Na_2O	6·75	6·58	0·22	0·54	0·04	0·00	0·00	7·70	0·13	8·11	0·15	0·00	0·00	0·00	0·00
K_2O	4·61	4·60	0·11	0·00	0·00	0·00	0·00	4·13	0·17	4·86	0·09	0·00	0·00	0·00	0·00
P_2O_5	0·19	0·17	0·09	0·00	0·00	0·00	0·00	0·00	0·00	0·00	0·00	0·00	0·00	0·00	0·00
BaO				0·00	0·00	0·00	0·00	0·63	0·04	0·24	0·17	0·00	0·00	0·00	0·00
Sum	100·19	100·00	0·00	99·24	0·92	98·20	1·95	98·69	0·96	99·58	0·44	93·75	0·01	96·91	0·01
PI	1·06	0·98													
Mg#															
Fa (mol %)						70·38	0·50								
Wo				43·17	0·33										
En				28·08	0·57										
Fs				28·75	0·59										
An								4·80	0·33	2·67	0·79				
Ab								70·39	0·95	69·79	0·49				
Or								24·82	0·92	27·54	0·70				

	PCD Bulk-rock	Starting material	SD	Cpx	SD	Ol	SD	Afs pheno	SD	Afs microlite	SD	Mt	SD	Ilm	SD
n:		20		8		6		10							
SiO_2 (wt %)	63·78	64·42	0·43	48·79	0·59	30·72	0·63	64·64	2·02						
TiO_2	0·75	0·68	0·14	0·57	0·20	0·00		0·06	0·06						
Al_2O_3	15·83	15·90	0·22	0·79	0·40	0·00		19·23	1·12						
FeO_{tot}	5·61	5·40	0·31	16·15	0·85	54·84	2·83	0·40	0·20						
MnO	0·19	0·20	0·08	0·98	0·14	2·79	0·30	0·05	0·06						
MgO	0·52	0·59	0·03	10·28	0·62	10·47	2·51	0·01	0·01						
CaO	1·87	2·06	0·08	20·41	0·19	0·41	0·10	1·59	1·48						
Na_2O	6·63	6·01	0·32	0·46	0·20	0·00		7·49	0·73						
K_2O	4·22	4·38	0·11	0·00	0·02	0·00		4·03	1·76						
P_2O_5		0·15	0·07		0·04			0·02	0·04						
BaO		0·12	0·06					0·20	0·16						
Sum		100·00	0·00	98·42	0·90	99·24	0·68	97·71	1·01						
PI	0·97	0·92	0·04												
Mg#															
Fa (mol %)						71	3·4								
Wo				43·76	1										
En				30·68	3										
Fs				25·56	3										
An								7·96	3						
Ab								67·99	2						
Or								24·05	5						

n, number of analyses; SD, standard deviation; FeO_{tot}, total iron reported as FeO. Ol, olivine; Cpx, clinopyroxene; Afs, alkali feldspar, Mt, magnetite; Ilm, ilmenite. Fa (mol %) = 100Mg/(Mg + FeO_{tot}) in olivine. Wo, En and Fs were calculated as in the study by Morimoto (1989). PI = peralkalinity index [molar $(Na_2O + K_2O)/Al_2O_3$]. An = 100[Ca/(Ca + Na + K)]; Ab = 100[Na/(Ca + Na + K)]; Or = 100[K/(Ca + Na + K)]. End-members calculated as in the study by Deer *et al.* (1992).

and Ol is $Fo_{23–27}$. In GTT Ilm has a TiO_2 content of 44·1% and Mt has an FeO content of 66·1 wt %.

The choice of experimental conditions was guided by the results of previous investigations carried out at Pantelleria. The range of pressures explored in this study reflects broadly the low pressure inferred on petrological grounds for the magma reservoir at Pantelleria (≤2 kbar; Di Carlo *et al.*, 2010; Gioncada & Landi, 2010; Neave *et al.*, 2012), which is typical of this category of magmas (Mahood, 1984; Scaillet & Macdonald, 2001, 2006). Temperature constraints come from the results of White *et al.* (2009) for the metaluminous trachyte (900 ± 50°C) filling the Cinque Denti Caldera, and from those estimated with the few analysed oxide pairs in GTT in this study. Using the formulation of Sauerzapf *et al.* (2008), the latter give a temperature of 932 ± 68°C and an fO_2 of NNO − 1·31 ± 0·09 (i.e. 1·31 log units below the Ni–NiO buffer). The low-temperature experiments were performed to investigate the relationships between trachyte and pantellerite.

EXPERIMENTAL STRATEGY

Charge preparation

The rocks chosen as starting materials were initially crushed and about 10 g of the resulting powders were fused twice in a Pt crucible at 1300°C in air for 3–4 h. Glass chips were analysed by electron microprobe and found to be homogeneous and similar to the bulk-rock analyses of the natural rocks (Table 1), the small differences (Na in particular) being due to the high melting temperature needed to prepare the starting material from the natural rock. The glasses were then ground in an agate mortar under acetone to 10–40 μm mesh size and utilized as starting materials for the experiments. Au capsules (1·5 cm in length, inner diameter 2·5 mm and outer diameter 2·9 mm) were used to minimize iron loss. Capsules were loaded first with distilled water, then silver oxalate as a CO_2 source, and finally with 30 mg of powdered glass. The amount of fluid ($H_2O + CO_2$) loaded into each capsule was $3 \pm 0{\cdot}5$ mg (10% of the starting material), ensuring always fluid saturation conditions (e.g. Scaillet *et al.*, 1995; Andújar *et al.*, 2015). Each capsule was arc-welded, with weighing before and after the welding to check for water loss; afterwards the capsules were left in an oven at 100°C to homogenize the water distribution within the capsule before the experiment and to check further for leaks. After the experiment, capsules were re-weighed and each capsule was considered successful if the pre-run–post-run weight difference was less than 0·4 mg, which is the precision of the analytical balance. Each run consisted of several capsules loaded together in the vessel, each capsule having a different H_2O/CO_2 ratio so as to vary XH_2O [= molar $H_2O/(H_2O + CO_2)$] between 1 and 0·12 (Table 2) at any explored P and T. Vesicle size and proportion vary with melt water content, and the presence of vesicles in all charges provides evidence for fluid saturation condition being attained at P and T.

Experimental equipment

All experiments were performed at the Institut des Sciences de la Terre d'Orléans using internally heated pressure vessels (IHPV) working vertically and equipped with either a molybdenum or a Kanthal furnace. The pressuring medium was an H_2–Ar mixture (loading sequentially H_2 and then Ar at room temperature), the Ar/H_2 ratio used to reach the desired target fO_2 being based on previous experiments (Scaillet *et al.*, 1992). Total pressure was recorded by a transducer calibrated against a Heise–Bourdon tube gauge (uncertainty ±20 bars), and temperature was continuously measured by two S-type thermocouples (accuracy ± 5°C). The fO_2 prevailing during the experiment was determined *a posteriori* through redox sensors, which consist of two pellets of hand-pressed Co–Pd–CoO powder loaded into Au capsules with distilled water, and embedded within ZrO_2 powder to prevent alloying with the Au (Taylor *et al.*, 1992). Run duration varied between 60 and 180 h (Table 2) depending on temperature. Experiments at $T > 800$°C were terminated using a drop-quench device (Di Carlo *et al.*, 2006), which allows a quench rate of >100°C s^{-1}. The transient increase in total pressure during the drop-quench was taken as evidence that the sample holder had successfully fallen into the bottom cold part of the vessel. Low-temperature experiments ($T \leq 800$°C) were terminated by switching off the power supply while maintaining the experimental pressure at the target value until about 300°C. After the experiment, the capsules were weighted to check for leaks and opened: some pieces of the run products were mounted in epoxy resin and polished for SEM–EDS (energy-dispersive spectrometry) phase identification and EMPA.

fH_2, fO_2 and water content in the experimental charges

The fO_2 recorded by the redox sensors allowed us to obtain the fH_2 at T–P during the experiment. This fH_2 was calculated from the water dissociation constant K_w $K_W(=f^\circ H_2O/fH2 * fO_2{}^{1/2}$ from Robie *et al.* (1997), using the $f^\circ H_2O$ (fugacity of pure water at P and T of interest; Burnham *et al.*, 1969) and the fO_2 of the sensor. For H_2O-saturated charges (i.e. $XH_2O = 1$), the fO_2 is that of the sensor. The fO_2 of each single H_2O-undersaturated charge was calculated using the water dissociation equilibrium, the fH_2 as given by the sensor, and the fH_2O of the charge, which was determined using the relationship $fH_2O = f^\circ H_2O \times XH_2O_{in}$ (moles). The fO_2 obtained using such a method ranges from NNO − 0·17 to NNO − 3·16, the spread reflecting essentially the fO_2 decrease with decreasing XH_2O (e.g. Scaillet & Evans, 1999; Di Carlo *et al.*, 2010; Cadoux *et al.*, 2014).

Most charges are characterized by high crystal contents preventing the use of techniques such as FTIR to determine directly the dissolved water content. Consequently, the water content in all charges was computed using the following approach. We first derived an empirical relationship between $f^\circ H_2O$ and H_2O content (at saturation) in the melt: $f^\circ H_2O = a(H_2O\ wt\ \%)^b$. To derive the a and b coefficients, we used the results of a series of supra-liquidus water-saturated experiments conducted on the sample GTT. The values determined are $a = 72{\cdot}612$ and $b = 1{\cdot}8615$. Then the H_2O_{melt} of each charge was computed from the equation H_2O_{melt} (wt %) $= (fH_2O/72{\cdot}612)^{1/1{\cdot}8615}$ (obtained by inverting the previous equation between fH_2O and H_2O_{melt}), where fH_2O is given by the relationship $fH_2O = f^\circ H_2O \times XH_2O_{in}$. It is important to note that this procedure is equivalent to assuming ideal behaviour in the H_2O–CO_2 fluid phase, so that the values obtained must be considered as maximum dissolved water contents. All results are listed in Table 2.

ANALYTICAL TECHNIQUES

A total of 68 charges were studied by SEM–EDS (Cambridge Leo 440 at University of Palermo and

Table 2: Experimental run conditions and results

Run	XH_2O_{in} (moles)*	H_2O_{melt} (wt %)†	log fO_2 (bar)‡	ΔQFM§	ΔNNO¶	Phase assemblage and abundances (wt %)	Crystal (wt %)	R^2
Green Tuff Trachyte (GTT)								
GT R9, 950°C, 1500 bar, PH_2‖ = 6·5 bar (target: FMQ buffer), 96 h								
1	1·00	4·95	−12·09	−0·47	−0·96	Gl only	0·7	1·07
2	0·81	4·42	−12·23	−0·61	−1·14	Gl only	0·0	0·78
3	0·52	3·47	−12·62	−1·00	−1·53	Gl (95·8), Cpx (1·1)	4·2	0·46
4	0·34	2·76	−12·99	−1·38	−1·91	Gl (97), Cpx (0·5)	3·0	0·42
5	0·10	1·44	−14·04	−2·43	−2·96	Gl (96·8), Cpx (0·3)	3·2	0·30
GT R7, 900°C, 1500 bar, PH_2 = 6·5 bar, 115 h								
1	1·00	4·95	−12·55	−0·10	−0·55	Gl (97·1), Cpx (0·1), Mt (3·4), Ilm (0·61)	2·9	0·31
2	0·82	4·46	−12·66	−0·21	−0·72	Gl (93·5), Cpx (3·7), Mt (6·83), Ilm (1·65)	6·5	0·45
3	0·53	3·54	−13·03	−0·58	−1·10	Gl (50·8), Cpx (3·5), Ol (2·3) Mt (2·9), Afs (40·5)	49·2	0·13
4	0·28	2·51	−13·58	−1·13	−1·65	Gl (36·0), Cpx (2·4), Ol (3), Mt (3·3), Afs (55·3)	64·0	0·27
GT R8, 850°C, 1500 bar, PH_2 = 6 bar, 125 h								
1	1·00	4·95	−13·73	−0·37	−0·77	Gl (94·3), Cpx (1·9), Mt (3·8)	5·7	0·81
2	0·82	4·47	−13·80	−0·44	−0·94	Gl (33·4), Cpx (5·2), Ol (0·4), Mt (4·9), Afs (56·1)	66·6	0·30
3	0·51	3·46	−14·21	−0·85	−1·35	Gl (24·2), Cpx (3·8), Ol (1·1), Mt (6·7), Afs (66·3)	75·8	0·46
4	0·33	2·75	−14·59	−1·22	−1·73	Gl, Cpx, Ol, Mt, Afs	n.d.	n.d.
5	0·10	1·44	−15·63	−2·27	−2·77	Gl, Cpx, Ol, Mt, Afs	n.d.	n.d.
GT R10, 950°C, 1000 bar, PH_2 = 5·5 bar, 96 h								
1	0·99	3·84	−12·06	−0·44	−1·00	Gl (97·8), Mt (2·2)	2·2	0·30
2	0·80	3·42	−12·28	−0·66	−1·19	Gl (98·3), Mt (1·7)	1·7	0·29
3	0·48	2·58	−12·73	−1·12	−1·64	Gl (96·5), Cpx (0·6), Ol (0·4), Mt (4·57), Ilm (2·04)	3·5	0·07
4	0·30	2·01	−13·14	−1·52	−2·04	Gl (96·0), Cpx (1·2), Ol (0·8), Mt (3·4), Ilm (1·3)	3·8	0·24
5	0·10	1·11	−14·09	−2·47	−3·00	Gl (68·0), Cpx (2·2), Ol (2·6), Mt (1·4), Afs (25·8)	32·0	0·15
GT R2, 900°C, 1000 bar, PH_2 = 5·5 bar, 86 h								
1	1·00	3·84	−12·52	−0·07	−0·59	Gl (97·1), Cpx (0·4), Mt (2·5)	2·9	0·39
2	0·80	3·41	−12·73	−0·28	−0·78	Gl (95·6), Cpx (0·9), Ol (0·4) Mt (3·1)	4·4	0·91
3	0·50	2·65	−13·13	−0·68	−1·19	Gl (75·2), Cpx (0·8), Ol (2·3) Mt (3·0), Afs (18·7)	24·8	0·19
4	0·30	2·01	−13·58	−1·13	−1·64	Gl (61·8), Cpx (1·0), Ol (3·0), Mt (2·2) Afs (32·0)	38·2	0·15
GT R4, 850°C, 1000 bar, PH_2 = 5·5 bar, 120 h								
6	1·00	3·84	−13·54	−0·18	−0·66	Gl (90·7), Cpx (3·6), Mt (5·7)	9·3	0·64
7	0·82	3·45	−13·71	−0·35	−0·84	Gl (48·9), Cpx (5·2), Ol (0·8), Mt (3·4), Afs (41·7)	51·1	0·07
8	0·51	2·66	−14·13	−0·76	−1·26	Gl (35·9), Cpx (2·3), Ol (1·7), Mt (3·7), Afs (56·7)	64·1	0·23
9	0·34	2·14	−14·48	−1·12	−1·61	Gl (30·2), Cpx (0·9), Ol (0·6), Mt (1·9), Afs (66·4)	69·8	0·94
10	0·10	1·11	−15·54	−2·17	−2·66	n.d.	n.d.	n.d.
GT R14, 800°C, 1000 bar, PH_2 = 6 bar, 150 h								
1	1·00	3·84	−14·68	−0·32	−0·75	Gl (25·2), Cpx (6·1), Ol (0·9), Mt (4·5), Afs (63·3)	74·8	0·14
2	0·82	3·46	−14·80	−0·45	−0·92	Gl (19·3), Cpx (7·3), Ol (0·5), Mt (4·7), Afs (69·2)	80·7	0·31
5	0·52	2·69	−15·21	−0·85	−1·33	Gl (18·7), Cpx (1·2), Ol (2·0), Mt (4·0), Afs (71·2)	81·2	1·83
GT R3, 750°C, 1000 bar, PH_2 = 5·5 bar, 170 h								
6	1·00	3·84	−15·74	−0·30	−0·66	Gl (23·8), Cpx (8·9), Ol (1·4), Mt (3·1), Afs (62·8)	76·2	0·20
7	0·10	1·11	−17·66	−2·21	−2·66	Gl, Cpx, Ol, Qz	100·0	nd
GT R11, 950°C, 500 bar, PH_2 = 5·5 bar, 96 h								
1	1·00	2·86	−12·22	−0·61	−1·12	Gl (98·7), Mt (1·3)	1·3	0·13
2	0·77	2·48	−12·45	−0·84	−1·35	Gl (97·9), Ol (0·7), Mt (1·4)	2·1	0·44
3	0·56	2·08	−12·73	−1·11	−1·63	Gl (97·6), Cpx (0·6), Ol (1·9), Mt (1·1)	2·4	0·30
4	0·37	1·67	−13·09	−1·47	−1·99	Gl (84·8), Cpx (0·6), Ol (3·5), Mt (0·13), Afs (12·2)	15·2	0·54
5	0·10	0·83	−14·22	−2·61	−3·12	Gl (75·9), Cpx (0·1), Ol (2·1), Mt (1·1), Afs (20·9)	24·1	0·06
GT R12, 900°C, 500 bar, PH_2 = 5·5 bar, 110 h								
1	1·00	2·86	−13·11	−0·66	−1·16	Gl (93·4), Cpx (1·6), Ol (1·5), Mt (3·5)	6·6	0·63
2	0·82	2·57	−13·28	−0·83	−1·33	Gl (93·3), Cpx (1·3), Ol (2·0), Mt (3·4)	6·7	0·78
3	0·71	2·37	−13·41	−0·96	−1·46	Gl (80·2), Cpx (2·2), Ol (2·5), Mt (1·4), Afs (13·7)	19·8	0·49
4	0·50	1·96	−13·72	−1·27	−1·76	Gl (54·2), Cpx (1·7), Ol (3·4), Mt (1·6), Afs (39·1)	45·8	0·28
5	0·30	1·51	−14·15	−1·69	−2·19	Gl (42·7), Cpx (0·5), Ol (3·0), Mt (2, 7), Afs (52·1)	57·3	0·22
6	0·10	0·83	−15·11	−2·66	−3·16	Gl, Cpx, Ol, Afs, Mt	nd	nd
Post Cinque Denti Caldera trachyte (PCD)								
R1, 950°C, 1500 bar, PH_2 = 6·5 bar (target: FMQ buffer), 60 h								
1	1·00	4·95	−11·45	0·16	−0·33	leaked		
2	0·80	4·41	−11·41	0·21	−0·28	Gl (97·2)	2·8	1·29
3	0·60	3·77	−11·66	−0·04	−0·54	Gl (95·7), Cpx (1·1) Mt (3·2)	4·3	1·35
4	0·45	3·23	−11·91	−0·29	−0·79	Gl (95·2), Cpx (1·5), Mt (3·3)	4·8	1·7
5	0·10	1·44	−13·22	−1·60	−2·09	Gl (54·3), Cpx (5·8), Ol (1·5), Mt (1·0), Afs (37·4)	45·7	0·12
R2, 900°C, 1500 bar, 96 h, PH_2 = 5·5 bar, 86 h								
1	1·00	4·95	−12·93	−0·47	−0·93	leaked		
2	0·80	4·40	−12·31	0·14	−0·38	Gl (94·3), Cpx (2·2), Mt (3·4)	5·6	0·94
3	0·57	3·68	−12·61	−0·15	−0·67	leaked		
4	0·46	3·28	−12·79	−0·34	−0·86	leaked		
5	0·10	1·44	−14·12	−1·67	−2·19	n.d.	∼100%	

(continued)

Table 2: Continued

Run	XH_2O_{in} (moles)*	H_2O_{melt} (wt %)†	log fO_2 (bar)‡	ΔQFM§	ΔNNO¶	Phase assemblage and abundances (wt %)	Crystal (wt %)	R^2
R4, 950° C, 1000 bar, PH_2 = 5·5 bar, 86 h								
1	1·00	3·84	−11·59	0·86	−0·53	Gl (100)	0	0
2	0·83	3·47	−11·79	0·66	−0·70	Gl (98), Cpx (2)	2	0·68
3	0·71	3·20	−11·92	0·53	−0·82	leaked		
4	0·45	2·50	−12·32	0·14	−1·22	Gl (62·4), Cpx (3·9), Mt (3·0) Afs (30·8),	37·6	0·82
5	0·10	1·11	−13·63	−1·17	−2·53	Gl (33·3), Cpx (6·6), Ol (3·2), Mt (3·0), Afs (60·4)	63·2	0·37
R3, 900° C, 1000 bar, PH_2 = 5·5 bar, 86 h								
1	1·00	3·84	−12·36	0·09	−0·43	leaked		
2	0·82	3·44	−12·61	−0·15	−0·66	Gl (95·4), Cpx (2·3), Mt (2·3)	4·6	1·13
3	0·58	2·86	−12·91	−0·45	−0·96	Gl (57·5), Cpx (4·0), Ol (1·9), Mt (1·7), Afs (34·9)	42·5	0·83
4	0·47	2·56	−13·09	−0·64	−1·14	Gl (39·4), Cpx (5·1), Ol (1·2), Mt (0·93), Afs (53·4)	60·6	0·52
5	0·10	1·11	−14·43	−1·98	−2·49	Gl, Cpx, Ol, Mt, Afs	n.d.	n.d.
R10, 850° C, 1000 bar, PH_2 = 6 bar, 120 h								
1	1·00	3·84	−13·54	−1·09	−0·66	Gl, Cpx, Mt, Afs	n.d.	n.d.
2	0·85	3·51	−13·04	−0·59	−0·17	Gl, Cpx, Ol, Mt, Afs	n.d.	n.d.
3	0·53	2·72	−13·45	−1·00	−0·58	Gl, Cpx, Ol, Mt, Afs	n.d.	n.d.
4	0·29	1·99	−13·96	−1·51	−1·09	Gl, Cpx, Ol, Mt, Afs	n.d.	n.d.

*XH_2O_{in}, initial mole fraction of H_2O of the C–H–O fluid loaded in the capsule.
†H_2O_{melt} (wt %), dissolved melt water content determined following the method of Scaillet & Macdonald (2006) and Andujar *et al.* (2016).
‡fO_2, logarithm of the oxygen fugacity (bar) calculated from the experimental fH_2 obtained from the solid sensors (see the text).
§ΔQFM, ¶ΔNNO log fO_2 – logfO_2 of the QFM and NNO buffer calculated at *P* and *T* respectively from Pownceby & O'Neill (1994) and Chou (1978).
‖PH_2, hydrogen pressure loaded in the vessel at room temperature. Crystal content, values indicate the phase abundance in the charge (in wt %). Gl, glass; Cpx, clinopyroxene; Ol, olivine; Mt, magnetite; Afs, alkali feldspar; Ilm, ilmenite; Qz, quartz.
'Leaked' indicates capsule that lost the fluid phase during the experiment.

Tescan Mira 3, XMU at ISTO-BRGM Orléans joint facility) for preliminary phase identification and textural analysis. Experimental phases and glasses were analysed by electron microprobe (CAMECA SX-Five at ISTO) using an acceleration voltage of 15 kV, sample current 6 nA and counting time of 10 s on peak and background for all elements; Na and K were analysed first and a ZAF correction was applied. Co–Pd–O solid sensors were analysed at 20 kV and 20 nA, with 10 s on each peak and 5 s on background. Mineral phases were analysed with a focused beam, whereas glasses were analysed with 10×10, 5×5 and 2×2 μm defocused beams (depending on the size of glass pools), as well as with a focused beam. Mineral and glass compositions in the natural rocks were determined using the same analytical conditions.

In our experimental glasses Na was affected by migration under the microprobe beam (e.g. Spray & Rae, 1995; Hanson *et al.*, 1996; Morgan & London, 1996, 2005). The local heating accompanied by the flux of beam energy is the most important factor in controlling Na mobility, which becomes severe in hydrous glasses and peralkaline compositions, where some fraction of the Na forms a terminal species on non-bridging O atoms associated with Si (Mysen, 1983; McMillan & Wolf, 1995; Morgan & London, 2005). As shown by Morgan & London (2005), using a current density close to 0·006 nA μm^{-2} the Na loss is lower than 2% in hydrous haplogranitic glass. For our analytical conditions, a current density close to 0·006 nA μm^{-2} corresponds to a 20×20 μm defocused beam, which was inappropriate for most of the experimental charges. Hence, to obtain reliable data on Na concentration of our experimental glasses, we calibrated the beam size effect (i.e. the current density) using different hydrous glass standards prepared from the starting material.

ATTAINMENT OF EQUILIBRIUM

The experimental strategy adopted in this work is well known for favouring crystal nucleation in aluminosilicate glasses (e.g. Clemens & Wall, 1981; Pichavant, 1987), as well as the attainment of crystal–liquid equilibrium on laboratory time-scales (Pichavant *et al.*, 2007). Previous studies performed on haplogranitic compositions (equivalent to high-silica rhyolites) have shown that crystal nucleation is promoted if a fine-grained dry glass is used as the starting material, as in our case. Our compositions are less silicic than the haplogranite one and richer in alkali elements. Both factors imply a lower melt viscosity and consequently component diffusivities significantly higher than in high-silica rhyolites for which crystal–liquid equilibrium has been demonstrated (e.g. Pichavant, 1987; Scaillet *et al.*, 1995).

As evidenced in other experimental studies on intermediate–felsic compositions (e.g. Martel *et al.*, 1999), when the drop-quench failed our compositions ended up producing abundant quench minerals showing that the activation energy for crystal nucleation was not insurmountable. More specifically, the experiments from this study are of crystallization-type and the condition of near-equilibrium crystallization reached in the experimental products is suggested by several observations,

in particular, (1) the euhedral shape of the crystals, (2) the homogeneous distribution of phases within the charges, (3) the low residuals of mass-balance calculations, and (4) the fact that crystal abundances and compositions vary regularly as a function of T and H_2O_{melt}. Altogether, this suggests that run durations were long enough (>60 h) to ensure close attainment of crystal–melt equilibrium, in agreement with previous work on broadly similar intermediate–felsic compositions (e.g. Martel *et al.*, 1999; Scaillet & Evans, 1999).

IRON LOSS TO THE CAPSULE MATERIAL

Iron loss to the capsule material is a severe problem with Pt and Au_{80}–Pd_{20} containers (Green & Ringwood, 1967), but less so when Au capsules are used (e.g. Sisson & Grove, 1993). In this study we did not observe large iron losses, except in charges GT R9-3, GT R9-4 and GT R-5, which were run at 950°C and in which estimated FeO loss ranges between 33 and 40%. In other charges run at the same temperature and similar fO_2 conditions, no iron loss was observed.

RESULTS

General observations

Our crystallization experiments show textural features similar to those observed in several crystallization experiments carried out at similar temperatures on intermediate to felsic compositions (e.g. Scaillet & Evans, 1999; Martel *et al.*, 1999, 2013; Cadoux *et al.*, 2014). Run products include mineral phases, glass and vesicles. Crystals have euhedral to sub-euhedral shapes: at $T > 900$°C their size ranges between 10 and 15 μm, whereas at lower temperature the size exceeds 10 μm (Fig. 2). The mineral phases identified are Cpx, Ol, Af, Mt, Ilm and Qz (the last only in charge GT R3-7). Glass was present in all charges except GT R3-7. In successfully drop-quenched runs, no evidence of quench textures was found, confirming that cooling rates were fast enough to prevent quench crystallization. Overall, crystallization experiments reproduce the natural phase assemblage observed in the targeted rocks.

Mineral and glass analyses were used in mass-balance calculations (Albarède, 1995) to obtain phase proportions for each charge (Table 2). Phase compositions are reported in Tables 3–7. The squared residuals of mass-balance calculations are generally < 1, suggesting that (1) no major phases were overlooked, (2) the Na contents of the experimental glasses have been correctly evaluated, and (3) iron loss to the capsule container was negligible. The variations of phase proportions with temperature and H_2O_{melt} are shown in Figs 3 and 4, respectively, and the phase relationships are shown in two projections of direct petrological use: T–H_2O_{melt} sections (Fig. 5) allow constrait of pre-eruptive conditions and the cooling history of trachytic magmas, whereas isothermal P–H_2O_{melt} sections (Fig. 6) show the effect of decreasing P and H_2O_{melt} on crystallization during magma ascent.

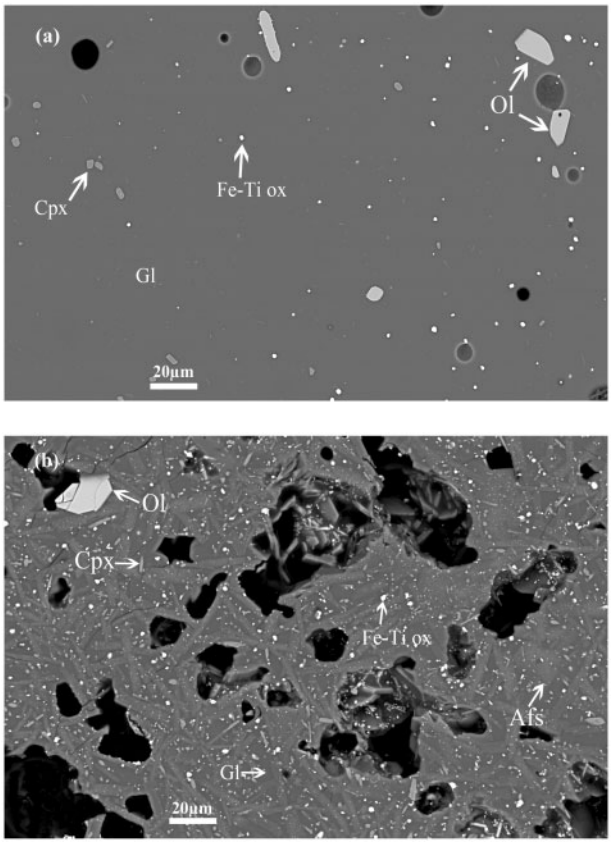

Fig. 2. Selected scanning electron microscope images of run products obtained in crystallization experiments at (a) 950°C, 1 kbar, $H_2O_{melt} = 3$ wt % and (b) 800°C, 1 kbar and H_2O_{melt}-saturated conditions. Ol, olivine; Cpx, clinopyroxene; Fe–Ti ox, Fe–Ti oxides; Afs, alkali feldspar; Gl, glass.

The experiments produced homogeneous phases and variations of the main intensive variables T, XH_2O and fO_2 are well displayed in the compositions of solid-solution phases. For example, small changes in fH_2O (i.e. H_2O_{melt}) produce variations in fO_2 that affect all iron-bearing minerals (i.e. Cpx, Ol and oxides). Microprobe analyses of Af were difficult to achieve owing to the poor contrast in back-scattered electron (BSE) images with residual glasses. Moreover, Af often contains small oxide inclusions, which increase its iron content. Some iron-rich analyses were recalculated assuming a maximum iron content of 1·5 wt % and subtracting the average composition of Mt. Both Mt and Ilm were always small (< 8 μm) and in some cases glass contamination during EMPA was inevitable. When glass contamination was reasonably low, the glass contribution was calculated out, otherwise Fe–Ti analyses were not considered. Similarly, the analysis of residual glasses in some crystal-rich charges was not possible even with a focused beam.

Phase proportions

Phase proportions obtained from mass-balance calculations show that the amount of glass in the run products

Table 3: Composition of experimental clinopyroxenes (wt %)

Run	*n*	SiO_2	TiO_2	Al_2O_3	FeO_{tot}	MnO	MgO	CaO	Na_2O	K_2O	P_2O_5	Total	*X*Fe
Green Tuff Trachyte (GTT)													
GT R9, 950° C, 1500 bar													
3	1	52·11	0·90	1·18	9·27	1·16	13·79	20·00	0·57	0·10	0·01	98·98	0·27
5	5	52·36	0·83	1·01	10·96	1·26	13·75	19·09	0·42	0·10	0·00	99·69	0·31
SD		0·26	0·23	0·42	1·08	0·23	0·62	0·82	0·15	0·07	0·00	0·55	0·03
GT R7, 900° C, 1500 bar													
1	6	52·38	0·50	0·69	11·83	1·10	12·79	19·84	0·42	0·07	0·03	99·66	0·34
SD		0·46	0·13	0·21	0·68	0·11	0·44	0·31	0·07	0·03	0·04	0·44	0·02
2	7	51·77	0·52	1·29	14·00	1·39	11·05	18·68	0·64	0·12	0·02	99·48	0·42
SD		0·51	0·17	0·42	1·64	0·17	0·63	0·69	0·08	0·04	0·04	0·49	0·04
3	7	51·54	0·59	1·59	19·35	1·46	8·49	15·96	0·75	0·42	0·06	100·20	0·56
SD		0·29	0·19	0·63	1·78	0·28	0·64	0·55	0·21	0·28	0·04	1·41	0·01
4	2	49·82	0·49	0·65	21·15	1·52	8·86	15·76	0·59	0·06	0·05	98·95	0·57
SD		0·82	0·01	0·21	0·62	0·06	0·21	0·68	0·09	0·00	0·00	0·20	0·06
GT R8, 850° C, 1500 bar													
1	3	52·95	0·24	1·40	14·38	1·60	10·38	19·16	0·53	0·02	0·01	100·67	0·44
SD		0·51	0·06	0·11	1·53	0·57	0·34	0·54	0·25	0·04	0·06	0·79	0·03
2	7	53·46	0·68	3·90	15·89	1·48	7·26	15·67	1·25	0·20	0·03	99·09	0·54
SD		1·15	0·35	0·63	1·17	0·17	0·67	0·97	0·15	0·20	0·09	1·24	0·03
3	6	50·19	0·66	1·22	21·97	1·93	6·45	15·46	0·80	0·13	0·08	98·81	0·67
SD		0·76	0·16	0·33	1·86	0·43	0·31	0·91	0·12	0·11	0·18	0·70	0·02
4	3	50·63	0·52	2·48	29·31	1·67	4·48	10·80	0·93	0·47	0·28	99·51	0·79
SD		0·29	0·16	0·42	0·62	0·62	0·21	0·09	0·15	0·20	0·00	0·63	0·05
GT R10, 950° C, 1000 bar													
3	11	52·29	0·51	1·23	13·66	1·21	11·66	18·75	0·51	0·18	0·08	99·82	0·40
SD		0·61	0·11	0·44	0·99	0·15	0·34	0·81	0·12	0·13	0·09	0·00	0·02
4	15	51·71	0·71	1·22	14·68	1·22	11·12	18·26	0·49	0·14	0·03	99·41	0·43
SD		0·82	0·12	0·88	1·14	0·20	0·76	1·04	0·28	0·10	0·05	0·96	0·02
5	7	52·14	0·82	1·41	18·56	1·60	9·62	15·48	0·56	0·26	0·29	100·19	0·52
SD		1·40	0·29	0·93	2·01	0·23	0·76	1·94	0·08	0·13	0·11	1·07	0·04
GT R2, 900° C, 1000 bar													
1	4	51·10	0·49	1·19	12·40	1·19	12·20	20·10	0·60	0·09	0·03	99·40	0·36
SD		0·87	0·12	0·12	0·90	0·40	0·32	0·87	0·13	0·02		0·90	0·02
2	10	52·02	0·43	1·71	13·79	1·25	11·59	18·78	0·65	0·22	0·03	100·47	0·40
SD		0·89	0·12	0·87	1·05	0·48	0·34	0·89	0·11	0·18	0·04	1·32	0·02
3	5	50·82	0·81	1·51	19·68	1·75	10·27	15·54	0·54	0·13	0·14	101·19	0·53
SD		0·61	0·87	0·27	1·67	0·12	0·42	1·26	0·16	0·03	0·08	0·39	0·03
4	5	50·67	0·59	1·15	20·72	1·65	8·78	15·26	0·65	0·26	0·10	99·48	0·57
SD		0·62	0·12	0·39	1·95	0·28	0·41	0·98	0·17	0·10	0·17	1·31	0·01
GT R4, 850° C, 1000 bar													
6	10	51·48	0·49	1·57	13·04	1·42	10·83	19·13	0·96	0·00	0·00	98·92	0·40
SD		0·92	0·33	0·97	1·11	0·41	0·72	0·32	0·20	0·07	0·05	1·49	0·03
7	2	50·78	0·54	2·58	16·99	1·56	8·35	16·04	1·43	0·02	0·03	98·34	0·53
SD		0·58	0·17	1·09	0·28	0·28	0·99	0·29	0·54	0·54	0·18	0·80	0·02
8	6	50·24	0·52	1·18	24·37	1·93	6·62	13·41	0·96	0·02	0·03	1·32	0·67
SD		0·95	0·34	0·37	1·44	0·47	0·21	1·33	0·23	0·19	0·33	0·78	0·01
9	1	49·58	0·73	1·50	27·64	1·70	5·16	13·32	1·30	0·40	0·06	100·92	0·75
SD		0·58	0·41	0·97	0·28	0·21	0·32	0·21	0·16	0·00	0·00	0·90	
GT R14, 800° C, 1000 bar													
1	4	51·54	0·95	4·01	16·56	1·83	7·61	15·43	1·69	0·49	0·05	100·32	0·55
SD		0·87	0·23	1·40	0·93	0·32	0·92	1·23	0·24	0·30	0·10	0·70	0·03
2	4	52·52	0·44	2·73	24·72	1·89	6·00	11·83	1·60	0·68	0·12	102·40	0·70
SD		0·99	0·05	0·58	0·54	0·18	0·24	0·82	0·43	0·30	0·10	52·52	0·01
5	5	49·86	0·38	1·41	26·86	2·07	5·66	11·31	1·04	0·33	0·11	99·12	0·73
SD		1·01	0·01	0·49	0·66	0·20	0·40	1·65	0·41	0·15	0·14	0·70	0·02
GT R3, 750° C, 1000 bar													
6	3	50·05	1·27	3·61	21·48	1·54	5·70	12·66	2·00	0·60	0·11	99·01	0·68
SD		1·45	0·52	0·94	1·24	0·19	0·37	1·03	0·45	0·40	0·09	1·33	0·07
GT R11, 950° C, 500 bar													
3	10	52·07	0·76	1·78	14·45	1·19	11·38	17·67	0·67	0·19	0·20	99·98	0·41
SD		1·20	0·23	0·69	0·98	0·14	0·44	0·90	0·27	0·06	0·07	0·90	0·01
4	13	52·31	0·71	1·63	15·73	1·29	10·82	16·94	0·53	0·35	0·02	99·95	0·45
SD		1·26	0·19	1·32	2·31	0·23	1·07	1·78	0·32	0·27	0·02	0·67	0·04
5	2	52·20	0·83	2·24	16·79	1·16	9·81	16·02	0·83	0·51	0·02	99·88	0·49
SD		1·62	0·07	1·49	2·10	0·05	0·58	0·59	0·69	0·32	0·02	1·75	0·02
GT R12, 900° C, 500 bar													
1	10	51·63	0·57	1·45	13·99	1·31	11·32	18·19	0·74	0·26	0·08	99·19	0·41
SD		1·19	0·34	0·87	1·47	0·13	0·34	0·66	0·34	0·18	0·13	1·51	0·02
2	11	52·44	0·43	1·00	15·77	1·50	10·95	17·65	0·47	0·15	0·08	100·21	0·45
SD		0·89	0·11	0·27	1·27	0·18	0·27	0·91	0·11	0·09	0·11	1·04	0·02

(continued)

Table 3: Continued

Run	*n*	SiO_2	TiO_2	Al_2O_3	FeO_{tot}	MnO	MgO	CaO	Na_2O	K_2O	P_2O_5	Total	*X*Fe
3	8	51·48	0·38	1·20	18·82	1·74	10·44	14·33	0·50	0·30	0·13	98·89	0·50
SD		0·58	0·10	0·23	0·68	0·18	0·26	0·65	0·13	0·09	0·07	0·58	0·01
4	7	52·24	0·42	1·67	19·66	1·68	8·88	14·15	0·87	0·44	0·15	99·57	0·55
SD		1·09	0·19	0·65	1·65	0·32	0·59	0·58	0·29	0·15	0·12	0·87	0·01
5	2	51·98	0·39	1·45	21·93	2·00	8·43	13·22	0·76	0·30	0·06	100·16	0·59
SD		0·11	0·24	0·41	0·07	0·10	0·14	1·46	0·09	0·00	0·00	0·78	0·00
Post Cinque Denti (PCD)													
R1, 950° C, 1500 bar													
3	6	51·14	0·75	1·93	15·36	0·84	10·31	19·64	0·49	0·16	0·16	100·79	0·45
SD		0·59	0·13	0·26	0·88	0·14	0·20	0·30	0·07	0·20	0·20	0·28	0·02
4	4	49·76	0·77	1·81	16·78	0·90	9·60	19·82	0·55	0·39	0·39	99·99	0·49
SD		0·39	0·10	0·14	1·03	0·08	0·14	0·28	0·05	0·26	0·26	0·50	0·01
5	4	50·78	0·67	1·99	23·59	1·36	7·48	14·14	0·77	0·37	0·05	100·79	0·64
SD		1·17	0·30	0·49	1·40	0·14	0·23	0·84	0·15	0·04	0·04	1·74	0·02
R2, 900° C, 1500 bar													
2	5	50·56	0·56	1·81	13·11	1·00	10·38	20·98	0·61	0·16	0·13	99·01	0·41
SD		0·89	0·08	0·49	0·66	0·17	0·17	0·44	0·10	0·32	0·04	1·04	0·01
R4, 950° C, 1000 bar													
2	4	51·83	0·59	1·91	13·41	0·78	10·79	20·06	0·56	0·22	0·10	99·93	0·41
SD		0·14	0·23	0·99	0·26	0·18	1·05	0·63	0·09	0·15	0·10	0·63	0·03
4	6	49·28	0·63	1·30	18·04	1·20	10·23	17·25	0·51	0·16	0·05	98·64	0·50
SD		0·47	0·19	0·32	1·17	0·10	0·52	1·08	0·10	0·11	0·08	0·65	0·03
5	2	48·53	0·86	2·20	22·03	1·52	8·20	15·23	0·66	0·30	0·04	99·56	0·60
SD		1·77	0·20	0·28	1·85	0·05	0·63	2·08	0·22	0·29	0·06	0·82	0·03
R3, 900° C, 1000 bar													
2	4	51·13	0·48	1·41	14·79	0·92	10·24	20·16	0·48	0·10	0·04	99·74	0·45
SD		0·62	0·16	0·37	0·52	0·19	0·23	0·31	0·09	0·04	0·04	0·60	0·01
3	5	50·36	0·45	0·94	21·35	1·63	9·15	15·35	0·46	0·14	0·11	99·92	0·57
SD		0·82	0·10	0·25	1·02	0·09	0·27	1·05	0·08	0·17	0·11	0·64	0·01
4	3	49·70	0·50	1·09	24·28	1·68	7·45	14·17	0·49	0·55	0·04	99·94	0·65
SD		0·67	0·16	0·62	2·58	0·23	0·89	0·84	0·12	0·08	0·07	1·04	0·05

n, number of analyses; SD, standard deviation; FeO_{tot}, total iron reported as FeO; *X*Fe, molar Fe/(Fe + Mg) in clinopyroxene.

varies from 98 wt % to less than 20 wt %, decreasing with decreasing H_2O_{melt} and temperature. Liquidus conditions were attained at 950°C and $H_2O_{melt} \geq 3{\cdot}5$ wt %, whereas the highest crystal contents (~80 wt %) were obtained at temperatures ≤800°C (Fig. 3a). At 750°C and nominally dry conditions no glass was detected in the charge and we consequently infer that the H_2O-saturated solidus for the trachytic magma is close to this temperature (a small amount of water is probably present because of the reduction of Fe_2O_3 by the hydrogen of the pressure medium, which produces enough water to saturate the system). In charges where Af does not crystallize, the crystal content never exceeds 12 wt %. Af, whenever present, increases linearly as the melt fraction decreases, becoming rapidly the dominant mineral phase (Fig. 3b). At any given temperature and pressure, the amount of Af tends to increase with decreasing H_2O_{melt}, but a large increase in Af content is also observable when temperature decreases (Fig. 4a, Table 2). Cpx never exceeds 9 wt % whereas the amount of Ol is usually below 4 wt %. The Af/Cpx + Ol ratios of the experimental charges broadly bracket those of the natural rocks, which are around 4–6 (Fig. 4b). Fe–Ti oxide abundances range between 2 and 5 wt %. It is worth noting that the experiments performed on both starting materials show the same phase proportion variation with respect to *P*–*T*–H_2O_{melt}. The small compositional difference between the two starting materials affects the crystal contents, and, under similar *P*–*T*–H_2O_{melt} conditions, PCD charges have a slightly higher crystal content than those of GTT (Fig. 4a).

Phase relationships

Phase relationships are shown in Figs 5–7. The GTT phase equilibria were established between 750 and 950°C and 0·5 and 1·5 kbar, whereas for PCD narrower ranges of temperature (850–950°C) and pressure (1·0–1·5 kbar) were explored (Table 2). Isobaric phase relationships as a function of temperature and H_2O_{melt} are shown at 1·5, 1, and 0·5 kbar for GTT and at 1·5 and 1 kbar for PCD, and the effect of decreasing pressure is shown at 950°C (Fig. 7). In both compositions, the stability fields of Cpx, Ol and Af are well defined, whereas oxide stability fields are constrained only in broad outline. At 1·5 kbar, Mt is always present in charges below 950°C, whereas Ilm occurs sporadically only in a few charges. Below, we describe in detail the phase relationships for each composition.

Green Tuff trachytic member (GTT)

At 1·5 kbar, Cpx is the liquidus phase appearing at 950°C and $H_2O_{melt} < 4$ wt %. At 900°C Cpx becomes stable at H_2O-saturation at all investigated pressures and is followed by Ol, then by Af when H_2O_{melt} is lower than 3·5 wt % (Fig. 5a). Ilm and Mt appear at $T < 950$°C

Table 4: Composition of experimental olivines (wt %)

Run	*n*	SiO_2	TiO_2	Al_2O_3	FeO_{tot}	MnO	MgO	CaO	Na_2O	K_2O	P_2O_5	Total	Fa mol %
Green Tuff (GTT)													
GT R7, 900° C, 1500 bar													
2	4	33·16	0·03	0·02	46·78	2·98	15·45	0·33	0·03	0·03	0·16	98·96	60·49
SD		0·27	0·04	0·04	0·29	0·06	0·28	0·01	0·03	0·05	0·22	0·45	0·27
3	6	32·11	0·05	0·03	51·33	3·17	9·97	0·49	0·03	0·00	0·00	97·57	71·14
SD		0·53	0·13	0·33	0·87	0·19	0·31	0·10	0·10	0·08	0·11	1·09	0·59
4	3	30·78	0·13	0·04	56·37	3·32	8·78	0·43	0·04	0·04	0·24	100·19	74·77
SD		0·06	0·08	0·05	0·61	0·16	0·08	0·08	0·04	0·03	0·26	0·75	0·33
GT R8, 850° C, 1500 bar													
2	8	31·38	0·22	0·07	51·73	3·58	8·44	0·34	0·07	0·07	0·17	95·76	73·48
SD		0·44	0·17	0·03	0·65	0·42	0·17	0·05	0·08	0·05	0·14	0·97	0·54
3	5	31·04	0·04	0·12	53·43	3·42	6·59	0·33	0·12	0·08	0·18	95·40	77·83
SD		0·82	0·90	0·73	0·95	0·29	0·78	0·05	0·34	0·18	0·16	0·75	1·44
4	4	30·72	0·10	0·09	57·51	2·70	4·44	0·32	0·04	0·10	0·12	96·15	84·36
SD		0·19	0·05	0·16	0·83	0·19	0·19	0·03	0·03	0·08	0·08	0·71	0·33
GT R10, 950° C, 1000 bar													
3	12	33·65	0·00	0·00	43·36	2·46	17·23	0·36	0·01	0·00	0·00	97·42	57·37
SD		0·42	0·04	0·12	0·87	0·31	0·37	0·04	0·03	0·07	0·16	0·83	0·31
4	12	33·42	0·02	0·01	44·22	2·73	16·50	0·40	0·00	0·00	0·00	97·70	58·45
SD		0·34	0·09	0·04	0·70	0·12	0·55	0·08	0·08	0·04	0·19	0·68	1·02
5	2	32·56	0·00	0·00	48·85	3·00	12·17	0·00	0·00	0·00	0·20	99·70	70·71
SD		0·77	0·04	0·03	0·93	0·36	1·22	0·14	0·02	0·02	0·12	1·05	0·47
GT R2, 900° C, 1000 bar													
2	7	32·90	0·01	0·00	46·64	2·95	16·81	0·31	0·05	0·02	0·19	100·29	59·05
SD		0·35	0·04	0·02	0·79	0·19	0·40	0·03	0·03	0·02	0·09	0·93	0·74
3	6	32·02	0·18	0·11	49·96	3·11	12·15	0·38	0·07	0·06	0·16	97·75	66·63
SD		0·51	0·09	0·44	1·05	0·21	0·29	0·03	0·06	0·10	0·19	1·40	0·56
4	5	32·43	0·14	0·30	51·00	2·60	9·59	0·46	0·10	0·21	0·15	96·52	71·59
SD		0·52	0·08	0·17	0·69	0·64	0·68	0·09	0·08	0·15	0·09	0·63	0·12
GT R4, 850° C, 1000 bar													
7	7	31·32	0·10	0·04	52·73	3·76	9·40	0·28	0·04	0·08	0·27	98·03	71·93
SD		0·40	0·09	0·05	1·84	0·43	0·59	0·04	0·07	0·05	0·21	1·95	0·86
8	5	30·86	0·13	0·01	56·89	3·22	6·34	0·30	0·06	0·02	0·13	97·41	79·61
SD		0·76	0·07	0·01	0·85	0·20	0·40	0·06	0·04	0·03	0·16	0·50	0·78
9	2	32·92	0·05	0·03	57·13	2·95	5·09	0·35	0·03	0·00	0·00	98·55	85·10
SD		1·23	0·15	0·28	2·39	0·03	0·56	0·02	0·24	0·03	0·08	0·01	1·67
GT R14, 800° C, 1000 bar													
1	9	31·33	0·05	0·02	52·61	3·84	7·30	0·25	0·04	0·07	0·15	95·39	75·69
SD		0·30	0·09	0·03	0·62	0·24	0·30	0·10	0·05	0·04	0·09	0·42	0·80
2	1	31·66	0·04	0·30	56·11	3·67	6·72	0·24	0·19	0·12	0·13	97·14	77·99
SD		0·60	0·06	0·48	1·07	0·47	1·11	0·05	0·21	0·12	0·10	0·00	0·90
5	3	31·14	0·06	0·01	55·90	3·31	4·43	0·27	0·06	0·05	0·13	95·36	83·26
SD		0·27	0·06	0·02	0·94	0·28	0·40	0·03	0·03	0·06	0·12	0·83	0·73
GT R3, 750° C, 1000 bar													
6	5	30·70	0·26	0·43	58·11	3·06	5·26	0·25	0·14	0·12	0·23	98·03	82·32
SD		1·12	0·40	0·70	1·65	0·08	0·18	0·07	0·17	0·11	0·08	1·59	0·27
7	2	31·49	0·12	0·72	59·17	2·23	3·04	0·34	0·41	0·19	0·03	97·73	88·53
SD		2·01	0·03	0·93	2·65	0·30	0·24	0·17	0·58	0·23	0·05	1·21	0·62
GT R11, 950° C, 500 bar													
2	2	33·40	0·04	0·07	40·14	2·61	20·36	0·32	0·04	0·08	0·15	97·20	50·75
SD		1·09	0·01	0·05	0·28	0·06	0·10	0·05	0·01	0·01	0·04	1·35	0·25
3	7	33·73	0·28	0·04	43·38	2·50	18·05	0·37	0·04	0·08	0·19	98·66	55·55
SD		0·73	0·37	0·04	1·09	0·17	0·64	0·01	0·04	0·03	0·22	0·56	1·28
4	8	32·35	0·08	0·05	46·42	2·59	14·69	0·44	0·06	0·08	0·22	96·98	61·70
SD		1·24	0·10	0·02	0·60	0·23	0·43	0·04	0·07	0·05	0·17	0·87	0·94
5	3	32·30	0·11	0·01	49·91	2·87	13·03	0·45	0·03	0·07	0·16	97·84	65·63
SD		1·70	0·05	0·03	1·22	0·24	0·18	0·03	0·04	0·07	0·09	0·60	1·70
GT R12, 900° C, 500 bar													
1	2	33·64	0·05	0·01	44·09	3·11	17·34	0·32	0·01	0·05	0·22	98·85	56·42
SD		0·28	0·08	0·01	0·67	0·17	0·44	0·05	0·02	0·05	0·15	0·11	1·03
2	7	33·31	0·07	0·02	45·92	3·27	14·95	0·37	0·05	0·06	0·13	98·15	60·52
SD		0·70	0·07	0·03	1·18	0·18	0·77	0·07	0·03	0·04	0·09	0·74	1·63
3	5	33·08	0·07	0·04	47·92	3·35	12·93	0·38	0·06	0·05	0·14	98·01	64·44
SD		0·38	0·07	0·04	0·63	0·20	0·45	0·05	0·05	0·03	0·08	0·55	0·70
4	6	32·13	0·06	0·04	51·00	3·35	10·05	0·41	0·07	0·08	0·19	97·37	70·54
SD		1·31	0·06	0·03	0·78	0·23	0·35	0·05	0·10	0·04	0·09	1·04	0·57
5	7	32·08	0·15	0·06	52·27	3·38	9·05	0·46	0·06	0·05	0·22	97·76	72·78
SD		0·42	0·11	0·07	1·10	0·28	0·93	0·08	0·05	0·06	0·10	0·33	1·40

(continued)

Table 4: Continued

Run	*n*	SiO_2	TiO_2	Al_2O_3	FeO_{tot}	MnO	MgO	CaO	Na_2O	K_2O	P_2O_5	Total	Fa mol %
Post Cinque Denti Caldera (PCD)													
R1, 950°C, 1500 bar													
5	4	31·59	0·11	0·17	55·57	2·70	8·57	0·85	0·06	0·11	0·57	100·30	75·00
SD		0·69	0·05	0·25	1·10	0·08	0·50	0·45	0·06	0·09	0·55	0·71	0·68
R4, 950°C, 1000 bar													
5	7	31·01	0·05	0·18	55·62	2·62	10·00	0·44	0·06	0·08	0·12	100·19	73·00
SD		0·62	0·04	0·18	0·54	0·15	0·67	0·09	0·04	0·02	0·12	0·97	1·17
R3, 900°C, 1000 bar													
3	5	31·96	0·03	0·14	54·38	2·93	9·48	0·47	0·05	0·09	0·10	99·38	73·00
SD		0·44	0·03	0·20	0·90	0·20	0·34	0·21	0·04	0·08	0·08	1·53	0·47
4	5	30·84	0·10	0·06	57·97	3·00	6·65	0·43	0·05	0·08	0·12	99·05	80·00
SD		0·55	0·09	0·06	0·47	0·17	0·31	0·07	0·03	0·04	0·04	0·63	0·42

n, number of analyses; SD, standard deviation; FeO_{tot}, total iron reported as FeO; Fa (mol %) = 100Fe/(Fe_{tot} + Mg + Mn) in olivine.

regardless of H_2O_{melt}. Cpx, Ol and Fe–Ti oxide are the liquidus phases at 1 kbar, 950°C and H_2O_{melt} close to 3 wt %, followed by Af for $H_2O_{melt} \leq 2{\cdot}5$ wt %. The Af stability field expands with decreasing temperature, becoming stable at H_2O-saturation at $T \leq 800$°C (Fig. 5b). At 0·5 kbar and 950°C, Ol replaces Cpx as the liquidus phase (Fig. 5c), becoming stable at H_2O saturation at 900°C. The isothermal P–H_2O_{melt} projections show that a near-isothermal ascent at either 950°C or 900°C (Fig. 6a and b) promotes crystallization and consequently an increase in crystal content with decreasing melt water content.

Post Cinque Denti Caldera trachyte (PCD). The phase diagrams for PCD show some differences from those of GTT (Fig. 7a). At 1·5 kbar, 950°C and $H_2O_{melt} < 4$ wt % Cpx is the liquidus phase, being followed by Ol and Af at $H_2O_{melt} < 3$ wt %. Phase relationships at 1·0 kbar (Fig. 7b) show that Cpx is the liquidus phase, as observed in GTT (Fig. 5b), but is followed first by Af, then by Ol. Af displays the same behaviour as in GTT, but at H_2O-saturation it becomes stable at a slightly higher temperature, around 850°C. The effect of pressure is shown in the isothermal section at 950°C (Fig. 7c); again, it is apparent that a near-isothermal ascent of such a trachytic melt would also promote crystallization of the three principal mineral phases.

Phase compositions

Experimental mineral phases of both compositions studied are similar, and they are reported in Tables 3–7. The variation with P–T–fO_2 and H_2O_{melt} of the GTT experimental phases is shown in Figs 8–13 and discussed below.

Clinopyroxene

Experimental Cpx is augite with compositions in the range $En_{26–42}$–$Fs_{17–58}$–$Wo_{26–42}$ and XFe [= Fe/(Fe + Mg), calculated using FeO_{tot}] ranging between 0·27 and 0·75 (Table 3). Compositional trends of experimental Cpx are governed by variation in T, H_2O_{melt} and fO_2. At a given temperature, the Wo content of Cpx decreases by 10 mol % when H_2O_{melt} decreases by 1·5–2 wt %, whereas the Fs content shows the opposite behaviour (Fig. 8a and b). Cpx becomes progressively richer in Na_2O and FeO_{tot} and poorer in Mg with melt evolution (and hence with decreasing temperature and H_2O_{melt}) (Fig. 8c and d). At 950°C, XFe ranges between 0·27 and 0·50. whereas below 850°C it reaches values up 0·75, displaying a good correlation with H_2O_{melt} and fO_2 (Fig. 8e). The average Cpx liquid exchange coefficient $Kd^{Fe–Mg}$ (calculated with FeO = FeO_{tot}) is 0·15 ± 0·06. This value is similar to that found by Di Carlo *et al.* (2010) and Scaillet & Macdonald (2003). The covariation of $X$$Fe_{tot}$ with temperature, fO_2, pressure and H_2O_{melt} can be parametrized with the following empirical equation:

$$XFe = -0{\cdot}0024xT(^{\circ}C) + 0{\cdot}0002xP(bar) - 0{\cdot}2044xH_2O_{melt}(wt\ \%) + 0{\cdot}0718x\Delta NNO + 3{\cdot}117 \quad (R^2 = 0{\cdot}92). \quad (1)$$

Equation (1) back-calculates experimental XFe to within ±0·02. Owing to its empirical nature, the use of such an equation, and of all similar equations that follow, is strictly recommended only for compositions similar to those of the Pantelleria trachytes.

Olivine

The composition of Ol falls in the range Fo_{46}–Fo_{12} [calculated as Mg/(Fe + Mg + Mn)] and can be classified as ferrohortonolite (Table 4). In the experimental P–T–H_2O_{melt}–fO_2 range explored, the highest Fo contents were reached at 950°C, whereas the lowest Fo contents occur at 750°C and low fO_2 (Fig. 9). As for Cpx, Ol composition varies systematically with temperature, H_2O_{melt} and fO_2, becoming Fe-rich with melt evolution. The most Fe-rich Ol occurs in low-H_2O_{melt} or low-temperature charges (i.e. $T < 850$°C), where Af dominates over Cpx and Ol. The composition of experimental Ol is strongly affected by H_2O_{melt} and consequently by fO_2. At constant P and T, a decrease of 1·5 wt % in

Table 5: Composition of experimental alkali feldspars (wt %)

Run	*n*	SiO2	TiO_2	Al_2O_3	FeO_{tot}	MnO	MgO	CaO	Na_2O	K_2O	P_2O5	Total	An–Or (%)
Green Tuff (GTT)													
GT R7, 900° C, 1500 bar													
3	3	65·84	0·22	18·10	1·12	0·02	0·07	0·97	7·61	4·75	0·10	99·02	5·88–26·33
SD		1·21	0·06	1·20	0·61	0·06	0·06	0·26	0·36	0·23	0·09	0·43	
4	1	64·48	0·38	16·31	3·07	0·20	0·21	1·08	7·44	4·79	0·03	97·87	6·35–27·85
GT R8, 850° C, 1500 bar													
2		68·48	0·30	17·83	1·37	0·14	0·15	0·89	6·76	4·99	0·22	101·12	4·65–31·18
SD		1·05	0·01	0·36	0·76	0·10	0·07	0·06	0·74	0·45	0·12	0·00	
3		68·00	0·15	17·79	1·31	0·12	0·30	1·22	6·88	5·06	0·19	101·03	6·20–30·57
SD		0·21	0·03	0·34	0·06	0·00	0·06	0·39	0·25	0·29	0·01	0·16	
GT R10, 950° C, 1000 bar													
5	2	64·78	0·31	19·02	1·05	0·02	0·04	1·04	8·01	4·33	0·00	98·60	6·82–24·54
SD		0·27	0·29	0·20	0·20	0·00	0·02	0·00	0·24	0·30	0·00	0·92	
GT R2, 900° C, 1000 bar													
3	5	65·09	0·44	18·46	1·25	0·07	0·35	1·88	7·51	3·54	0·17	98·96	9·57–21·39
SD		1·72	0·17	0·37	1·35	0·06	0·12	0·37	0·82	0·25	0·22	0·85	
4	10	64·96	0·50	18·72	1·00	0·00	0·05	2·00	7·50	4·01	0·13	98·87	9·78–21·23
SD		1·30	0·10	0·51	0·92	0·06	0·13	0·33	0·41	0·14	0·01	0·67	
GT R4, 850° C, 1000 bar													
7	8	66·44	0·51	17·96	1·59	0·15	0·06	0·67	7·40	4·75	0·06	99·58	3·41–28·69
SD		1·64	0·19	0·79	1·06	0·08	0·06	0·21	0·81	0·35	0·06	1·75	
8	2	65·97	0·23	17·98	1·32	0·09	0·45	1·53	7·93	4·64	0·09	99·56	7·13–25·80
SD		0·16	0·04	0·20	0·44	0·08	0·16	0·28	0·59	0·25	0·13	1·71	
9	1	66·77	0·17	16·71	1·32	0·11	0·47	1·64	7·62	4·46	0·17	97·83	7·90–25·61
GT R14, 800° C, 1000 bar													
1	4	67·34	0·20	18·10	1·66	0·03	0·06	0·71	7·60	4·18	0·10	100·64	3·34–28·84
SD		0·49	0·25	0·67	0·76	0·05	0·05	0·22	0·18	0·00	0·09	1·28	
2	4	65·29	0·58	17·47	5·11	0·16	0·24	1·03	7·24	4·14	0·14	99·43	4·62–27·12
SD		0·51	0·07	0·35	0·24	0·10	0·07	0·31	0·18	0·43	0·09	0·99	
5	2	65·66	0·76	16·32	4·71	0·05	0·56	1·70	6·16	0·00	0·07	100·26	10·79–25·59
		0·35	0·09	0·24	0·38	0·15	0·08	0·28	0·45	0·38	0·00	0·70	
GT R3, 750° C, 1000 bar													
6	7	66·67	0·24	18·58	0·89	0·05	0·09	0·23	7·95	5·35	0·16	98·38	2·42–28·82
SD		1·01	0·06	0·60	0·20	0·02	0·02	0·32	0·44	0·75	0·22	0·79	
GT R11, 950° C, 500 bar													
4	2	64·29	0·21	18·15	0·74	0·20	0·11	1·92	7·55	3·68	0·08	96·93	9·69–21·48
SD		0·27		0·08	0·19	0·06	0·03	0·41	0·45	0·37	0·03	0·10	
5	5	63·85	0·11	19·05	1·39	0·02	0·06	1·88	7·79	3·51	0·10	97·75	9·32–20·72
SD		0·37	0·08	0·27	0·94	0·03	0·03	0·45	0·41	0·40	0·02	0·05	
GT R12, 900° C, 500 bar													
3	1	64·33	0·44	18·31	2·30	0·18	0·48	0·48	7·70	4·19	0·03	99·86	9·29–23·90
4	3	64·91	0·50	18·30	2·88	0·09	0·41	0·41	7·50	4·00	0·04	100·32	9·51–25·12
SD		2·14	0·14	0·26	0·63	0·01	0·10	0·10	0·36	0·35	0·02	1·50	
5	2	65·86	0·00	17·82	1·41	0·08	0·36	1·96	7·34	4·00	0·15	100·00	9·82–23·80
SD		1·97	0·03	0·32	0·38	0·03	0·14	0·14	0·54	0·05	0·10	2·09	
Post Cinque Denti (PCD)													
R1, 950° C, 1500 bar													
5	2	65·53	0·17	19·52	0·64	0·00	0·00	1·09	7·60	4·42	0·02	99·21	5·4–26·1
SD		0·37	0·00	1·50	1·16	0·00	0·00	0·27	1·17	0·37	0·00	0·24	
R4, 950° C, 1000 bar													
4	3	65·80	0·13	19·52	0·61	0·30	0·80	1·02	7·80	4·91	0·00	100·89	4·9–27·9
SD		0·44	0·07	0·71	0·70	0·09	0·08	0·20	0·34	0·55	0·00	0·40	
5	4	63·29	0·26	17·95	1·63	0·02	0·06	1·19	7·79	4·25	0·04	96·48	4·70–24·7
SD		0·71	0·09	0·44	0·57	0·00	0·01	0·21	0·44	0·62	0·02	0·30	
R3, 900° C, 1000 bar													
3	6	64·19	0·10	19·03	0·65	0·04	0·01	1·38	8·30	3·98	0·05	97·72	6·51–22·41
SD		0·64	0·07	0·27	0·18	0·04	0·01	0·20	0·42	0·34	0·06	0·57	
4	3	63·64	0·42	19·31	2·10	0·00	0·01	1·66	7·69	3·87	0·04	98·73	8·20–22·86
SD		0·04	0·07	0·99	0·03	0·03	0·03	0·08	0·47	0·01	0·32	1·08	

n, number of analyses; SD, standard deviation; FeO_{tot}, total iron reported as FeO; An–Or (%), mol % of anorthite and orthoclase of the alkali feldspar.

H_2O_{melt} (i.e. the average variation of water content along a given isothermal experimental series) produces a decrease of about 1·5–2 log units in fO_2 (Table 4), which is accompanied by a decrease in the fayalite content in Ol of 5–10 mol % (Fig. 9c and d). The average Ol–liquid exchange coefficient Kd^{Fe-Mg}, calculated considering $FeO = FeO_{tot}$, is $0{\cdot}37 \pm 0{\cdot}12$, which is broadly similar to the *K*d of previous studies (e.g. Sisson & Grove, 1993; Pichavant *et al.*, 2002; Barclay & Carmichael, 2004) although most of them concerned more Mg-rich Ol in equilibrium with more mafic melts.

Table 6: Composition of experimental magnetite and ilmenite

Run	*n*	SiO_2	TiO_2	Al_2O_3	FeO_{tot}	MnO	MgO	CaO	Na_2O	K_2O	P_2O_5	Total	% Ulv
Green Tuff Magnetite (GTT)													
GT R7, 900° C, 1500 bar													
1	2	0·46	19·58	1·09	66·34	1·54	1·45	0·12	0·04	0·10	0·46	90·58	60·5
SD		0·31	0·40	0·05	0·83	0·08	0·06	0·13	0·04	0·30	0·31	0·00	
2	1	1·16	20·15	1·39	65·66	1·49	1·36	0·20	0·03	0·05	1·16	91·40	64·73
GT R8, 850° C, 1500 bar													
1	2	0·82	15·74	1·32	68·73	1·58	0·78	0·07	0·00	0·00	0·00	89·04	50·99
SD		0·06	0·35	0·00	0·50	0·13	0·00	0·03	0·00	0·00	0·00	1·07	
GT R10, 950° C, 1000 bar													
1	7	0·26	18·35	1·34	68·38	1·38	1·59	0·05	0·03	0·11	0·01	91·48	57·59
SD		0·04	0·28	0·13	0·93	0·16	0·05	0·01	0·04	0·05	0·01	0·81	
2	8	0·34	21·14	1·35	65·65	1·48	1·82	0·09	0·02	0·12	0·06	92·08	65·29
SD		0·25	0·46	0·09	0·31	0·17	0·02	0·04	0·04	0·03	0·06	0·80	
3	2	1·06	23·17	1·53	64·25	1·44	1·69	0·06	0·13	0·14	0·02	93·50	72·71
SD		0·95	0·04	0·25	0·65	0·11	0·01	0·00	0·03	0·01	0·00	0·37	
5	1	0·44	26·33	0·74	63·47	2·20	1·26	0·05	0·00	0·23	0·10	94·82	78·71
GT R2, 900° C, 1000 bar													
1	6	0·66	17·98	1·37	71·09	1·47	1·72	0·08	0·03	0·04	0·02	94·36	53·47
SD		0·68	0·47	0·37	0·55	0·21	0·03	0·04	0·05	0·07	0·09	1·33	
2	2	0·26	19·42	1·22	69·36	1·33	1·56	0·13	0·03	0·04	0·02	93·27	57·83
SD		0·05	0·10	0·04	0·53	0·02	0·11	0·08	0·05	0·09	0·00	0·94	
GT R4, 850° C, 1000 bar													
6	1	2·00	15·43	2·20	67·57	1·84	0·90	0·07	0·27	0·38	0·02	90·69	59·3
SD													
7	3	0·24	19·58	1·09	66·34	1·54	1·45	0·12	0·00	0·03	0·02	90·41	61·98
SD		0·10	0·20	0·03	0·40	0·30	0·11	0·02	0·00	0·01	0·00	0·09	
GT R11, 950° C, 500 bar													
1	3	0·58	20·13	1·47	65·70	1·36	1·65	0·07	0·01	0·10	0·02	90·97	63·28
SD		0·26	0·34	0·09	1·14	0·28	0·02	0·02	0·20	0·10	0·02	0·00	
2	2	0·44	20·17	1·46	65·26	1·77	1·87	0·10	0·12	0·12	0·00	91·30	67·02
GT R12, 900° C, 500 bar													
1	1	0·18	18·24	1·35	69·20	1·40	1·40	0·07	0·00	0·13	0·03	92·00	55·34
3	3	1·98	17·47	1·93	72·48	1·41	1·31	0·19	0·02	0·09	0·06	96·94	55·1
		0·2	1·04	0·34	0·29	0·09	0·01	0·05	0·01	0·02	0·00	0·42	
Post Cinque Denti Magnetite (PCD)													
R2, 900° C, 1500 bar													
2	3	1·80	16·07	2·94	70·50	1·31	1·00	0·14	0·26	0·29	0·05	94·34	54·91
SD		0·54	0·35	0·17	0·29	0·23	0·06	0·10	0·08	0·06	0·04	0·66	
R4, 950° C, 1000 bar													
2	2	0·85	21·82	1·61	67·83	1·59	1·48	0·10	0·08	0·12	0·00	96·13	66·86
SD		0·02	0·21	0·01	1·42	0·03	0·02	0·01	0·05	0·10	0·00	1·96	
3	3	0·34	19·65	1·19	70·26	1·23	0·79	0·10	0·07	0·13	0·06	94·39	59·73
SD		0·15	0·07	0·06	0·82	0·31	0·02	0·02	0·03	0·03	0·03	0·60	
R3, 900° C, 1000 bar													
3	4	0·98	22·15	1·12	69·09	1·38	1·08	0·10	0·14	0·11	0·01	96·14	67·08
SD		0·25	1·23	0·14	1·26	0·12	0·12	0·06	0·11	0·05	0·02	1·92	
Green Tuff Ilmenite (GTT)													
GT R7, 900° C, 1500 bar													
1	4	0·14	48·62	0·08	41·14	2·04	2·21	0·07	0·05	0·07	0·00	94·29	96·04
SD		0·15	0·59	0·02	0·88	0·20	0·07	0·04					
2	2	1·31	48·11	0·28	41·40	2·07	2·10	0·17	0·21	0·18	0·00	95·83	96·91
SD		1·73	0·17	0·29	0·76	0·29	0·18	0·01	0·28	0·04	0·00	2·22	
GT R10, 950° C, 1000 bar													
3	3	1·76	48·15	0·62	39·73	1·98	2·67	0·12	0·07	0·25	0·00	95·02	98·51
SD		1·25	0·10	0·35	0·01	0·15	0·01	0·02	0·01	0·00	0·00	0·90	

n, number of analyses; SD, standard deviation; FeO_{tot}, total iron reported as FeO; % Ulv, mol % of ulvöspinel in the oxide; % Ilm, mol % of ilmenite in the oxide.

The influence of *T*, *P*, H_2O_{melt} and fO_2 on Ol composition has been parameterized with the following simple empirical equation:

$$Fa\ (mol\%) = -0{\cdot}1973xT(^{\circ}C) + 0{\cdot}0134xP(bar) + 1{\cdot}7118x\Delta NNO - 11{\cdot}9175xH_2O_{melt}(wt\ \%) + 262{\cdot}2215\ (R^2 = 0{\cdot}95). \quad (2)$$

Equation (2) back-calculates the Fa content of experimental olivines to within 1·2 mol %.

Alkali feldspar

Microprobe analyses of Af were considered acceptable when the structural formula fulfilled the following criteria: $3{\cdot}950 < (Si + Al + Fe) < 4{\cdot}050$ and $0{\cdot}950 < (Ca + Na + K) < 1{\cdot}050$ on an 8-oxygen basis. Analyses of Af are listed in Table 5. Af in single charges usually displays a small compositional variation of 1–3 mol % An, which is considered to be within the analytical uncertainty, given the problems mentioned above. In our

Table 7: Composition of experimental glasses

Run	*n*	SiO_2	TiO_2	Al_2O_3	FeO_{tot}	MnO	MgO	CaO	Na_2O	K_2O	P_2O_5	Total	PI
Green Tuff (GTT)													
GT R9, 950° C, 1500 bar													
1	7	65·23	0·95	15·24	5·34	0·35	0·65	1·54	6·46	4·55	0·29	100·00	1·02
SD		0·36	0·07	0·11	0·23	0·07	0·03	0·04	0·81	0·18	0·09	0·94	
2	7	65·48	0·78	15·70	5·09	0·20	0·58	1·11	6·34	4·38	0·34	100·00	0·97
SD		0·44	0·10	0·22	0·22	0·10	0·04	0·05	0·57	0·14	0·09	0·67	
3	7	66·57	0·85	15·96	3·35	0·18	0·66	1·35	6·35	4·59	0·14	96·97	0·97
SD		0·65	0·09	0·31	0·19	0·09	0·02	0·08	0·38	0·12	0·09	0·63	
4	7	65·97	0·87	15·75	3·89	0·28	0·66	1·43	6·21	4·67	0·27	100·00	0·97
SD		0·12	0·12	0·13	0·33	0·11	0·03	0·04	0·60	0·16	0·10	0·80	
5	7	66·05	0·94	15·84	3·45	0·24	0·69	1·48	6·35	4·77	0·19	100·00	0·98
SD		0·52	0·11	0·10	0·27	0·10	0·03	0·07	0·52	0·13	0·04	0·49	
GT R7, 900° C, 1500 bar													
1	20	66·26	0·63	15·34	4·51	0·20	0·59	1·38	6·38	4·59	0·11	100·00	1·01
SD		0·81	0·09	0·33	0·68	0·09	0·10	0·16	0·62	0·11	0·07	0·00	
2	5	67·62	0·47	15·75	3·41	0·13	0·31	0·82	6·49	4·91	0·08	100·00	1·02
SD		0·83	0·06	0·17	0·35	0·06	0·11	0·08	0·94	0·14	0·06	0·92	
3	3	68·52	0·38	14·81	3·79	0·04	0·16	0·68	6·44	5·05	0·14	100·00	1·08
SD		0·17	0·08	0·40	0·28	0·07	0·09	0·05	0·80	0·12	0·03	0·80	
4	1	70·25	0·49	13·34	3·37	0·00	0·33	0·85	6·42	4·80	0·15	100·00	1·18
GT R8, 850° C, 1500 bar													
1	1	67·16	0·39	15·60	3·76	0·15	0·15	1·10	6·22	5·07	0·40	100·00	1·01
SD		0·77	0·07	0·43	0·50	0·03	0·00	0·30	0·50	0·18	0·02	0·90	
2	3	68·34	0·56	14·59	3·85	0·17	0·12	0·45	6·74	5·08	0·09	100·00	1·14
SD		0·30	0·04	0·09	0·72	0·02	0·04	0·03	0·20	0·13	0·02	0·55	
3	3	69·85	0·30	13·94	3·10	0·07	0·14	0·82	6·74	4·64	0·38	100·00	1·16
SD		0·80	0·02	0·60	0·22	0·01	0·03	0·04	0·00	0·35	0·08	0·72	
GT R10, 950° C, 1000 bar													
1	8	65·62	0·77	15·46	4·79	0·24	0·60	1·33	6·33	4·65	0·21	100·00	0·99
SD		0·55	0·08	0·17	0·25	0·09	0·03	0·05	0·73	0·16	0·07	0·00	
2	7	64·99	0·87	15·28	4·93	0·28	0·64	1·40	6·73	4·66	0·22	100·00	1·05
SD		0·58	0·28	0·19	0·55	0·13	0·04	0·08	0·55	0·14	0·14	0·80	
3	13	65·90	0·77	15·67	3·99	0·16	0·54	1·42	6·70	4·63	0·22	100·00	1·02
SD		0·56	0·06	0·13	0·48	0·08	0·02	0·36	0·58	0·19	0·28	0·00	
4	6	65·87	0·75	15·80	4·30	0·16	0·44	1·35	6·72	4·73	0·19	100·00	1·02
SD		0·35	0·10	0·13	0·35	0·06	0·02	0·09	0·56	0·09	0·07	0·43	
5	1	66·65	0·68	14·68	4·80	0·22	0·35	1·00	6·36	5·09	0·16	100·00	1·09
GT R2, 900° C, 1000 bar													
1	5	65·72	0·56	15·72	4·62	0·21	0·59	1·48	6·33	4·57	0·20	100·00	0·97
SD		0·39	0·07	0·12	0·48	0·10	0·03	0·10	0·09	0·04	0·10	0·46	
2	4	66·38	0·42	15·74	4·43	0·23	0·55	1·37	6·22	4·54	0·12	100·00	0·96
SD		0·75	0·10	0·04	0·30	0·08	0·11	0·19	0·37	0·15	0·11	1·08	
3	3	67·61	0·48	15·35	3·35	0·07	0·30	1·13	6·50	4·95	0·26	100·00	1·05
SD		0·16	0·51	15·08	0·39	0·09	0·29	0·10	0·07	0·08	0·09	0·79	
4	3	67·69	0·56	14·59	4·27	0·19	0·27	0·91	6·29	4·98	0·25	100·00	1·08
SD		0·61	0·11	0·42	0·70	0·05	0·03	0·14	0·73	0·15	0·22	0·79	
GT R4, 850° C, 1000 bar													
6	4	68·69	0·23	15·83	2·30	0·22	0·14	0·65	7·24	4·67	0·03	100·00	1·07
SD		0·33	0·07	0·30	0·08	0·08	0·01	0·04	1·52	0·62	0·07	1·60	
7	5	69·34	0·19	15·11	3·07	0·04	0·13	0·49	6·80	4·81	0·01	100·00	1·09
SD		0·24	0·02	0·10	0·16	0·05	0·01	0·03	0·20	0·07	0·01	0·10	
8	2	70·21	0·64	13·10	4·13	0·12	0·19	0·53	6·48	4·51	0·09	100·00	1·19
SD		0·45	0·10	0·67	0·44	0·07	0·09	0·10	0·30	0·13	0·04	0·92	
9	2	70·33	0·44	12·80	3·94	0·32	0·38	1·07	6·22	4·22	0·27	100·00	1·16
SD		2·84	0·14	0·77	0·57	0·04	0·19	0·53	0·92	0·37	0·16	0·85	
GT R14, 800° C, 1000 bar													
1	8	71·28	0·27	13·52	2·87	0·22	0·11	0·43	6·55	4·72	0·03	93·00	1·17
SD		1·64	0·08	0·46	0·35	0·07	0·15	0·39	0·86	0·50	0·12	2·33	
2	1	71·54	0·34	12·95	2·94	0·15	0·17	0·74	6·52	4·22	0·45	92·59	1·18
5	2	72·75	0·31	11·84	3·61	0·15	0·13	0·78	6·14	3·96	0·33	100	1·22
SD		1·21	0·01	0·58	0·48	0·12	0·01	0·14	0·25	0·04	0·03	1·13	
GT R3, 750° C, 1000 bar													
6	8	70·77	0·56	12·10	4·66	0·04	0·20	0·73	6·09	4·29	0·56	100·00	1·21
SD		0·20	0·19	0·80	1·10	0·13	0·18	0·43	0·85	0·52	0·17	4·12	
GT R11, 950° C, 500 bar													
1	16	64·92	0·87	15·08	5·29	0·19	0·63	1·44	6·71	4·67	0·21	94·82	1·07
SD		0·62	0·07	0·32	0·31	0·08	0·04	0·06	0·26	0·09	0·09	0·98	
2	7	65·00	0·87	15·18	4·72	0·24	0·63	1·51	6·58	4·60	0·28	100·00	1·04
SD		0·70	0·05	0·19	0·29	0·13	0·03	0·13	0·12	2·17	0·11	1·51	
3	4	65·19	0·86	15·22	4·65	0·22	0·57	1·43	6·94	4·74	0·18	100·00	1·09

(continued)

Table 7: Continued

Run	*n*	SiO_2	TiO_2	Al_2O_3	FeO_{tot}	MnO	MgO	CaO	Na_2O	K_2O	P_2O_5	Total	PI
SD		0·38	0·04	0·23	0·38	0·11	0·11	0·19	0·09	0·26	0·08	0·58	
4	6	65·20	1·00	14·87	5·05	0·33	0·28	1·49	6·31	5·47	0·00	100·00	1·10
SD		0·35	0·19	0·49	0·27	0·09	0·08	0·14	0·20	0·20	0·20	0·43	
5	2	65·77	0·74	14·31	5·67	0·18	0·38	1·37	6·30	5·00	0·28	100·00	1·10
SD		62·54	0·81	14·61	4·90	0·25	0·61	1·31	6·27	4·29	0·13	95·71	
GT R12, 900° C, 500 bar													
1	7	67·17	0·65	16·06	2·94	0·18	0·40	1·04	6·44	4·96	0·16	100·00	0·99
SD		0·78	0·13	0·20	0·76	0·10	0·02	0·14	0·84	0·18	0·10	0·68	
2	5	67·39	0·63	15·83	3·02	0·21	0·33	1·03	6·37	5·05	0·14	100·00	1·01
SD		0·51	0·13	0·16	0·28	0·14	0·01	0·06	0·75	0·12	0·08	0·78	
3	1	66·26	0·69	15·71	4·02	0·15	0·36	0·94	6·37	5·43	0·07	100·00	1·04
4	4	67·91	0·90	14·55	3·62	0·25	0·31	0·77	6·34	5·25	0·11	100·00	1·11
SD		0·11	0·16	0·22	0·04	0·20	0·01	0·09	0·01	0·08	0·06	0·10	
5	2	68·18	0·58	13·24	5·26	0·17	0·21	0·89	6·32	4·92	0·21	100·00	1·19
SD		0·83	0·08	0·70	0·36	0·15	0·29	0·74	0·08	0·20	0·03	0·00	
Post Cinque Denti Caldera (PCD)													
R1, 950° C, 1500 bar													
2	10	66·72	0·74	15·55	3·87	0·14	0·56	1·88	6·10	4·37	0·08	100·00	0·95
SD		0·33	0·08	0·28	0·30	0·05	0·01	0·04	0·18	0·09	0·07	0·49	
3	10	67·10	0·70	15·75	3·42	0·18	0·43	1·72	6·49	4·45	0·11	97·49	0·98
SD		0·94	0·10	0·28	0·17	0·07	0·03	0·07	0·11	0·15	0·08	1·06	
4	10	67·35	0·71	15·72	3·26	0·18	0·37	1·52	6·05	4·51	0·11	100·00	0·94
SD		0·23	0·07	0·22	0·23	0·06	0·03	0·09	0·14	0·08	0·08	0·32	
5	3	67·10	0·62	15·29	4·14	0·19	0·25	1·31	6·07	4·93	0·10	98·41	1·00
SD		0·66	0·15	0·62	0·13	0·10	0·06	0·18	0·71	0·13	0·04	0·89	
R2, 900° C, 1500 bar													
2	9	67·51	0·41	15·93	3·12	0·12	0·29	1·45	6·42	4·58	0·17	100·00	0·97
SD		0·33	0·06	0·17	0·28	0·10	0·04	0·18	0·74	0·15	0·10	0·91	
R4, 950° C, 1000 bar													
1	20	66·12	0·74	15·32	4·72	0·19	0·56	1·96	5·87	4·39	0·13	100·00	0·94
SD		0·47	0·10	0·18	0·23	0·09	0·02	0·10	0·73	0·21	0·08	1·03	
2	20	65·23	0·78	15·95	4·65	0·22	0·56	1·93	6·15	4·37	0·16	100·00	0·93
SD		0·80	0·08	0·23	0·24	0·08	0·02	0·25	0·15	0·16	0·14	0·06	
4	10	67·45	0·69	15·12	3·46	0·16	0·37	1·34	6·46	4·81	0·17	100·00	1·05
SD		0·45	0·09	0·17	0·34	0·08	0·03	0·08	0·12	0·19	0·08	0·75	
5	4	68·53	0·79	13·97	3·64	0·18	0·31	0·91	6·07	5·41	0·18	100·00	1·13
SD		0·29	0·11	0·23	0·28	0·06	0·02	0·03	0·11	0·11	0·02	0·59	
R3, 900° C, 1000 bar													
2	15	66·84	0·56	15·81	3·81	0·18	0·33	1·41	6·45	4·54	0·09	100·00	0·98
SD		0·96	0·24	0·22	0·63	0·12	0·06	0·16	0·12	0·15	0·07	0·57	
3	12	68·25	0·44	15·02	3·23	0·15	0·24	1·09	6·33	5·11	0·15	100·00	1·06
SD		0·30	0·06	0·22	0·25	0·12	0·06	0·05	0·14	0·01	0·03	0·10	
4	5	69·72	0·39	13·28	4·05	0·13	0·18	0·88	6·16	5·10	0·12	100·00	1·18
SD		0·50	0·07	0·10	0·19	0·11	0·02	0·29	0·09	0·07	0·14	0·43	

n, number of analysis; SD, standard deviation; FeO_{tot}, total iron reported as FeO; PI, peralkalinity index.

experiments only anorthoclase feldspars crystallized, with compositions in the range $An_{2–10}Ab_{63–68}Or_{20–28}$ (Fig. 10a). In detail, the An content ranges between 10 mol % at 950°C and 2 mol % at 750°C, whereas the Or content ranges between 28 mol % at 750°C and 20 mol % at 950°C; that is, similar to those observed in other compositionally similar systems (e.g. Scaillet & Macdonald, 2003). At fixed *T*, Or in Af tends to increase whereas the An content decreases with increasing H_2O_{melt} (Fig. 10b and e); that is, defining an opposite trend to that observed in more Ca-rich compositions in which more An-rich plagioclase crystallizes as H_2O_{melt} increases (e.g. Martel *et al.*, 1999; Scaillet & Evans, 1999).

The compositional variation of Af with temperature and H_2O_{melt} has been parameterized with the following empirical equation:

$$An\ (mol\%) = 0{\cdot}0244xT(^{\circ}C) - 1{\cdot}3456xH_2O_{melt}(wt\%) - 10{\cdot}22855(R^2 = 0{\cdot}86). \quad (3)$$

The equation back-calculates the An content to within 0·6 mol %.

Fe–Ti oxides

In Table 6 are reported the analyses of Fe–Ti oxides after calculating out glass contamination and computing Fe^{3+} from formula constraints. Mt is present in almost all charges, but its small size prevented its analysis, whereas Ilm was analysed only in charges GT R7-1, GT R7-2 and GT R10-3. For both oxides, analyses having totals outside the 96·5–102% range were excluded. Contents of FeO_{tot} and TiO_2 in Mt are in the

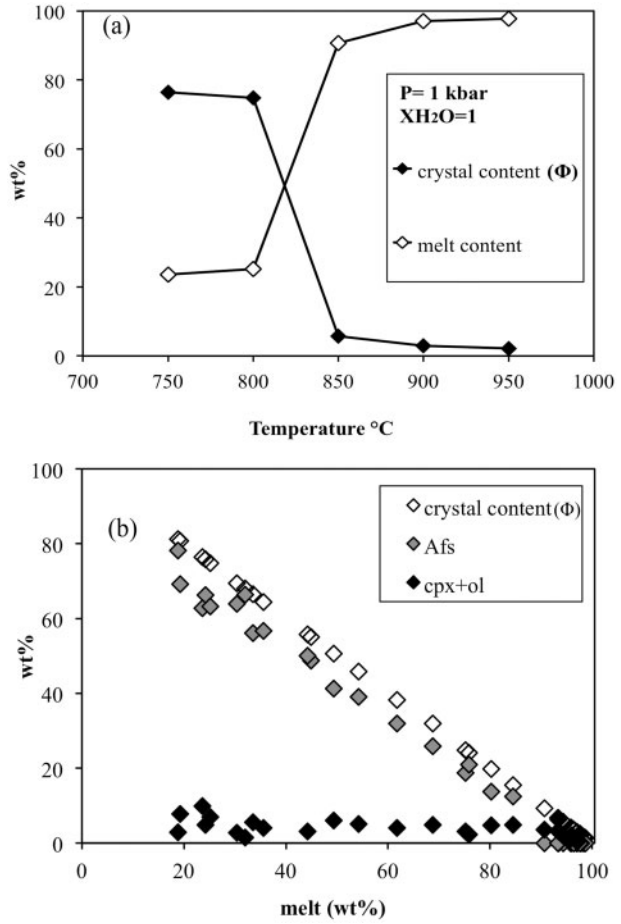

Fig. 3. (a) Variation of crystal and melt proportions with temperature at 1 kbar and $X\mathrm{H_2O}$ [$=\mathrm{H_2O}/(\mathrm{H_2O}+\mathrm{CO_2})$] $=$ 1 for GTT experiments. It should be noted that the increase in crystal content corresponds to the crystallization of alkali feldspar at $\mathrm{H_2O}$-saturation. (b) Variation of crystal, alkali feldspar and clinopyroxene (cpx) + olivine (ol) proportions as a function of melt per cent.

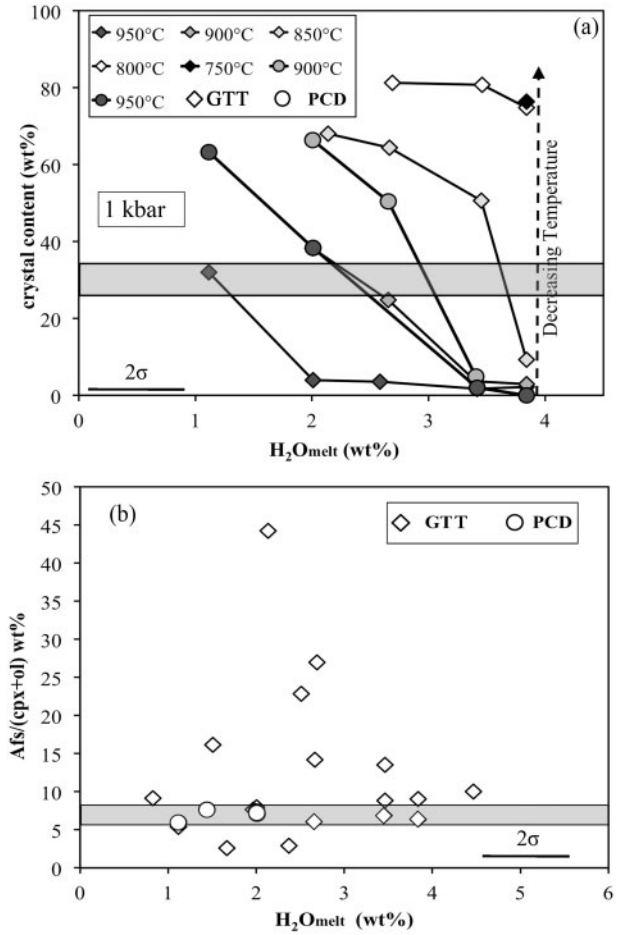

Fig. 4. (a) Variation of crystal content vs $\mathrm{H_2O_{melt}}$. The arrow indicates the large increase in crystal content when temperature decreases. (b) Variation of alkali feldspar/(clinopyroxene + olivine) ratio (wt %) in experimental charges. In both panels diamonds indicate experiments on the Green Tuff Trachyte (GTT), whereas circles show experiments on the Post Cinque Denti Caldera trachyte (PCD). The horizontal grey bar corresponds to the crystal content of both natural rocks.

range of 63·5–71·1 wt % and 15·4–26·3 wt % respectively, whereas in Ilm $\mathrm{FeO_{tot}}$ varies between 39·7 and 41·4 wt % and $\mathrm{TiO_2}$ is 48 ± 0·5 wt %. Contents of MnO and MgO are generally comparable with those in oxides in the natural rocks, whereas $\mathrm{Al_2O_3}$ is slightly higher. Ulvöspinel contents in Mt reflect changes in oxygen fugacity, decreasing when $f\mathrm{O_2}$ decreases. Needle-like Ilm and equant Mt usually coexist in charges at water-undersaturated conditions. Reliable analyses of coexisting Ilm and Mt were obtained only for three charges (GT R7-1, GT R7-2 and GT R10-3, Table 6). In these three charges there is an excellent agreement between the experimental T–$f\mathrm{O_2}$ conditions and those derived from coexisting oxides using the formulation of Sauerzapf *et al.* (2008); the formulation of Ghiorso & Evans (2008) tends instead to underestimate both temperature and oxygen fugacity (Fig. 11).

Glass

Glass (Gl) compositions of experimental charges recalculated on an anhydrous basis are listed in Table 7 and plotted in Fig. 12. At $T \geq 900$°C Gl compositions are close to those of the starting materials, evolving when melt fraction decreases with falling temperature and $\mathrm{H_2O_{melt}}$. Compositional changes with respect to T and $\mathrm{H_2O_{melt}}$ are obviously due to the crystallization of Cpx, Ol, Af and Fe–Ti oxides. Residual liquids are marked by a progressive increase in $\mathrm{SiO_2}$ with respect to the starting material (Fig. 12a), $\mathrm{SiO_2}$ content ranging from 65 to 73 wt % in the most crystallized charges. In near-liquidus charges, crystallization of Cpx, Ol and Fe–Ti oxides produces a decrease in $\mathrm{FeO_{tot}}$ and a slight increase in $\mathrm{Al_2O_3}$. The decrease of temperature and $\mathrm{H_2O_{melt}}$ promotes the massive crystallization of Af causing a decrease in $\mathrm{Al_2O_3}$ content, which drops from 15·7 wt % in near-liquidus charges to 11·8 wt % in crystal-rich charges (Fig. 12b). In contrast, the $\mathrm{FeO_{tot}}$ content, after a first decrease to 2·3 wt %, increases again to 4·7 wt % in some highly crystallized charges. This trend is more clearly illustrated in charges at 1 kbar, for which a large range of temperature was

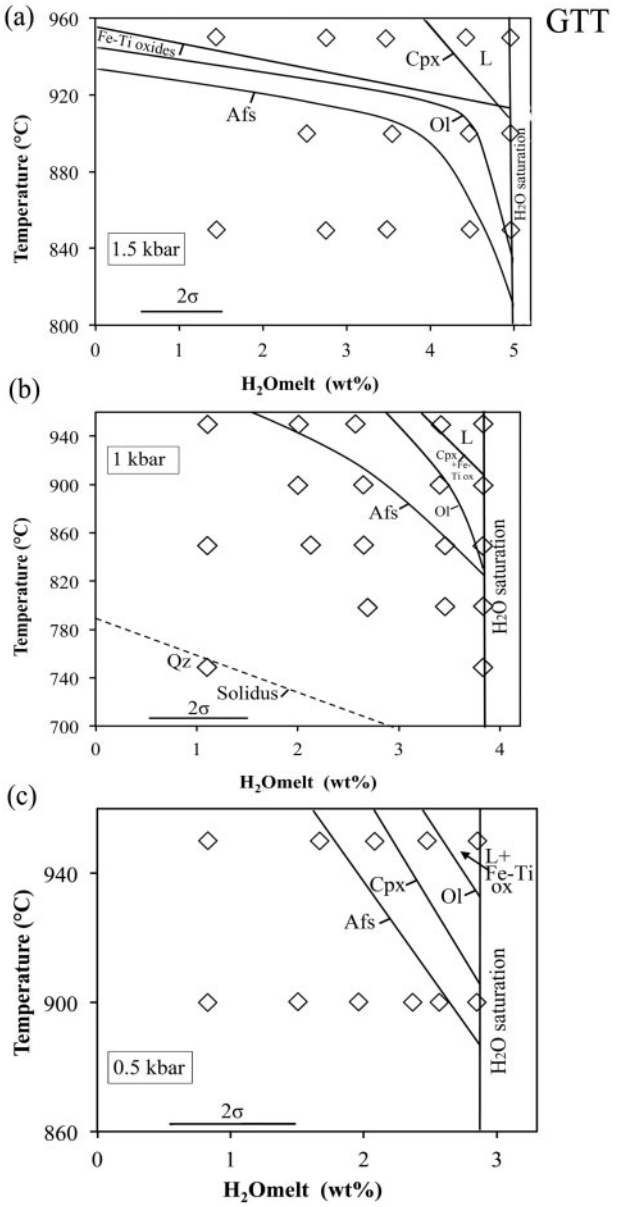

Fig. 5. Phase relationships of the Green Tuff Trachyte in T–H_2O_{melt} projections at (a) 1·5 kbar, (b) 1 kbar, and (c) 0·5 kbar, all at fO_2 ~NNO − 1. L, liquid; Cpx, clinopyroxene; Ol, olivine; Fe–Ti ox, Fe–Ti oxides; Afs, alkali feldspar; Qz, quartz. The tick on a phase boundary marks the side on which an experimental phase is stable. Dashed line is estimated phase boundary.

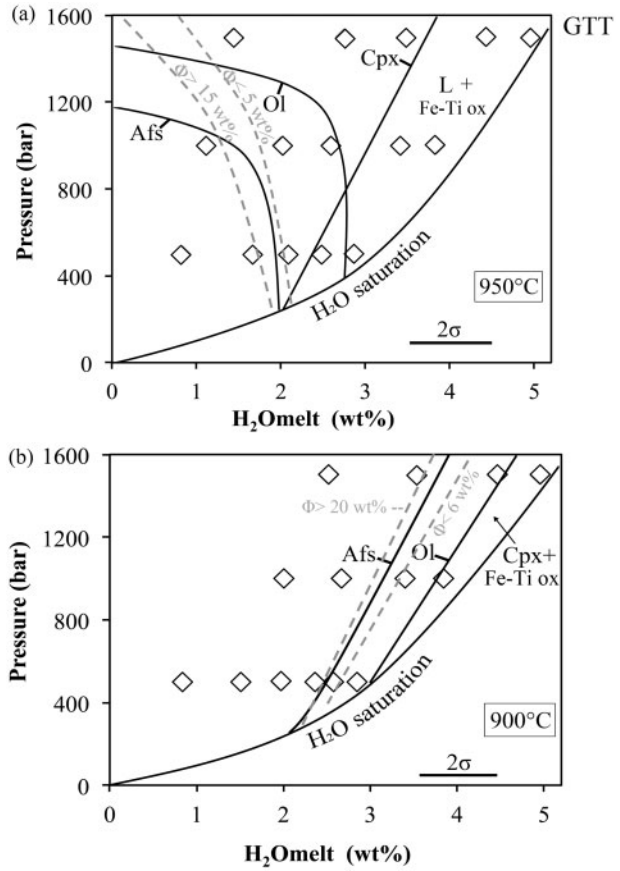

Fig. 6. Phase relationships of the Green Tuff Trachyte as a function of pressure and H_2O_{melt} at (a) 950°C, (b) 900°C and at fO_2 ~NNO − 1. L, liquid; Cpx, clinopyroxene; Ol, olivine; Fe–Ti ox, Fe–Ti oxides; Afs, alkali feldspar. The grey dashed lines indicate the crystal content (Φ, wt %).

explored. At this pressure and for $T < 850$°C the residual glass shows an increase in FeO_{tot} with crystallization, even if it remains lower than that of the starting material (see below). Other major elements (TiO_2, MnO, MgO, CaO) tend to decrease with crystallization (Fig 12d–f) whereas both Na_2O and K_2O remain roughly constant (5·5–6 wt % and 3·8–4·4 wt %, respectively). Variations in peralkalinity index (Fig. 12c) are thus primarily related to variations in Al_2O_3 content: when melt fraction decreases (i.e. at low temperature and low H_2O_{melt}) Al_2O_3 tends to decrease and the peralkalinity index increases up to 1·21 with respect to that of the starting material (0·98), i.e. residual liquid compositions are comenditic.

DISCUSSION

Comparison with other intermediate–felsic magmas

Intermediate–felsic magmas are characterized by variable silica contents, at ~62–68 wt % SiO_2. Dacitic and trachytic magmas have similar SiO_2 and Al_2O_3 contents but they differ in other major elements, in particular alkalis and MgO, CaO, and FeO_{tot} contents. These apparently small differences influence notably the stability of mineral phases. The range of temperature explored in our study is similar to that investigated to constrain the phase relationships of broadly similar trachytic magmas (Martel *et al.*, 2013) or common dacitic magmas, such as Pinatubo (Scaillet & Evans, 1999), San Pedro (Costa *et al.*, 2004) and the Fish Canyon Tuff (Johnson & Rutherford, 1989; Caricchi & Blundy, 2015) rocks. In contrast, the range of pressure and fO_2 explored in previous studies both tended to be higher, around 2–3 kbar and above the NNO buffer. Nevertheless, the liquidus temperature for dacitic magmas is constrained to be around 900–950°C for water contents between 4 and 6 wt %, similar to our findings.

In dacitic magmas (Pinatubo, San Pedro and Fish Canyon tuff dacites) a decrease in temperature from

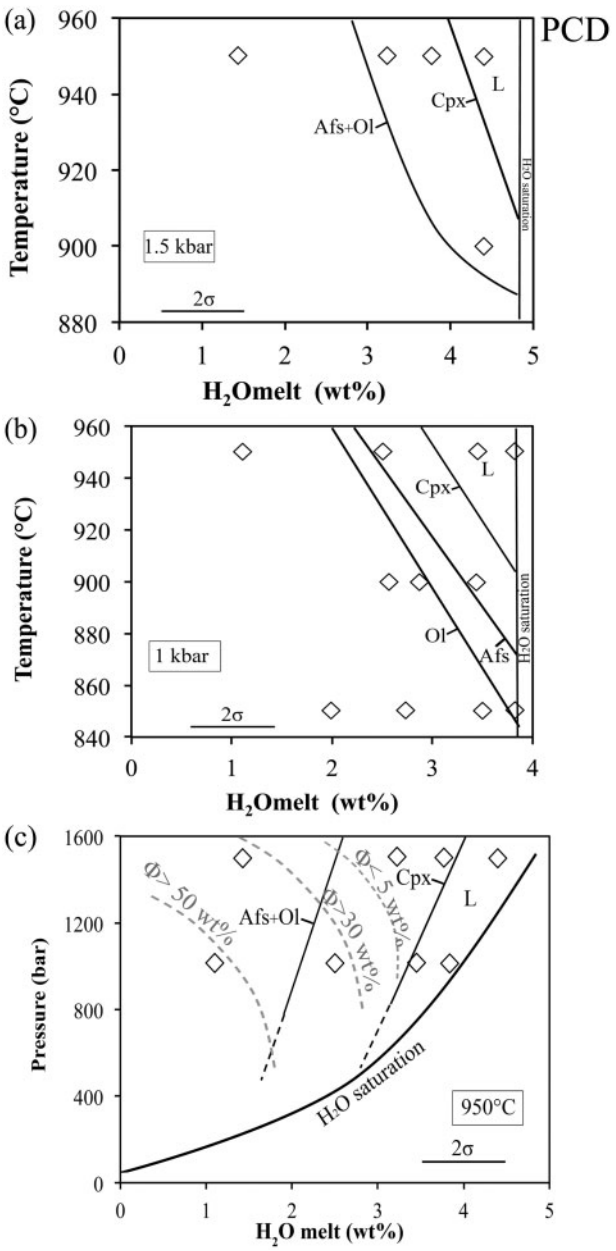

Fig. 7. Phase relationships of Post Cinque Denti Caldera trachyte at fO_2 ~NNO – 1 as a function of temperature and H_2O_{melt} at (a) 1·5 kbar, (b) 1 kbar and (c) pressure and H_2O_{melt} at 950°C. L, liquid; Cpx, clinopyroxene; Ol, olivine; Fe–Ti ox, Fe–Ti oxides; Afs, alkali feldspar. The tick on phase boundaries marks the side on which an experimental phase is stable. Dashed lines are estimated phase boundaries. The grey dashed lines indicate the crystal content (Φ, wt %).

950°C (near-liquidus conditions) to 800°C at H_2O_{melt} close to saturation (~7 wt % at 2 kbar) increases progressively the crystal content to 60 wt %. In our run products, for a similar decrease of temperature at H_2O saturation (~4 wt % at 1 kbar), the crystal content remains broadly constant (and low) until 850°C (0–10 wt %) but it rapidly increases to 75 wt % at temperature ≤800°C.

Similar behaviour is also observed in the experiments of Martel *et al.* (2013) wherein the crystal content increased to over 50 wt % only at $T \leq 750$°C and water saturation. At 900°C and 3 wt % H_2O_{melt} (i.e. undersaturated conditions) dacitic charges (Scaillet & Evans, 1999; Costa *et al.*, 2004) have crystal contents slightly higher than 50 wt %, whereas trachytic charges held at the same conditions have crystal contents close to 30 wt %. However, when the temperature decreases to 850°C both compositions end up with a crystal content ≥60 wt %. Further decreasing the temperature to 800°C, the dacite approaches its solidus (Scaillet & Evans, 1999), whereas for our trachyte at the same temperature and similar water content residual liquid is still present in a relatively large amount. Such a difference in temperature–melt fraction trends between metaluminous and peralkaline magmas has also been found for rhyolites (Scaillet & Macdonald, 2001, 2006; Di Carlo *et al.*, 2010). The lower solidus temperature of peralkaline systems suggests that they may survive (as molten bodies) for longer times in the cold upper crust compared with metaluminous magmas.

The mineral phases of trachytic and dacitic magmas present remarkable differences. The Pinatubo, San Pedro and Fish Canyon tuff dacites all crystallized plagioclase (Pl), Cpx and Mt as near-liquidus phases. In contrast, in trachytes Af is the only tectosilicate mineral phase (except for Qz crystallizing at near-solidus conditions). The absence of Pl in the GTT and PCD trachytes can be attributed to their lower CaO contents (~2 wt %) compared with that of dacitic magmas (~5 wt %). This has already been highlighted by the experiments of Martel *et al.* (2013), wherein small variation in the CaO content of trachytic starting compositions affected plagioclase stability. The presence of Af in dacitic magmas has been reported only at high degrees of melt evolution (i.e. low temperature and low melt water content; e.g. Scaillet & Evans, 1999). In our run products, Cpx is the liquidus phase, being stable at all temperatures investigated. However, in dacite magmas Cpx is stable only at $T \geq 800$°C (e.g. Scaillet & Evans, 1999; Costa *et al.*, 2004), whereas this phase persists below 800°C in trachytes (Martel *et al.*, 2013). Cpx stability may be related to the MgO/FeO_{tot} of the starting material, increasing when MgO/FeO increases. In trachytes *sensu lato* (this study; Martel *et al.*, 2013) this ratio is much lower than that of common dacitic magmas, and clinopyroxene is present over all the temperature range investigated even if, in detail, small variations in CaO and alkalis can affect the stability of Cpx (Martel *et al.*, 2013). The MgO and FeO_{tot} contents, and perhaps pressure, also control the stability of orthopyroxene (Opx), which has a large stability field in dacites, in particular in those with high MgO/FeO_{tot} ratios such as the Pinatubo dacite, whereas Opx is conspicuously absent in trachytes.

The high FeO (and low MgO) content in Pantelleria trachytes is highlighted by the occurrence of fayalitic Ol, a mineral phase common only in high-Fe intermediate and felsic magmas; that is, in Icelandic trachytes (Selbekk & Tronnes, 2007) and Yellowstone rhyolites

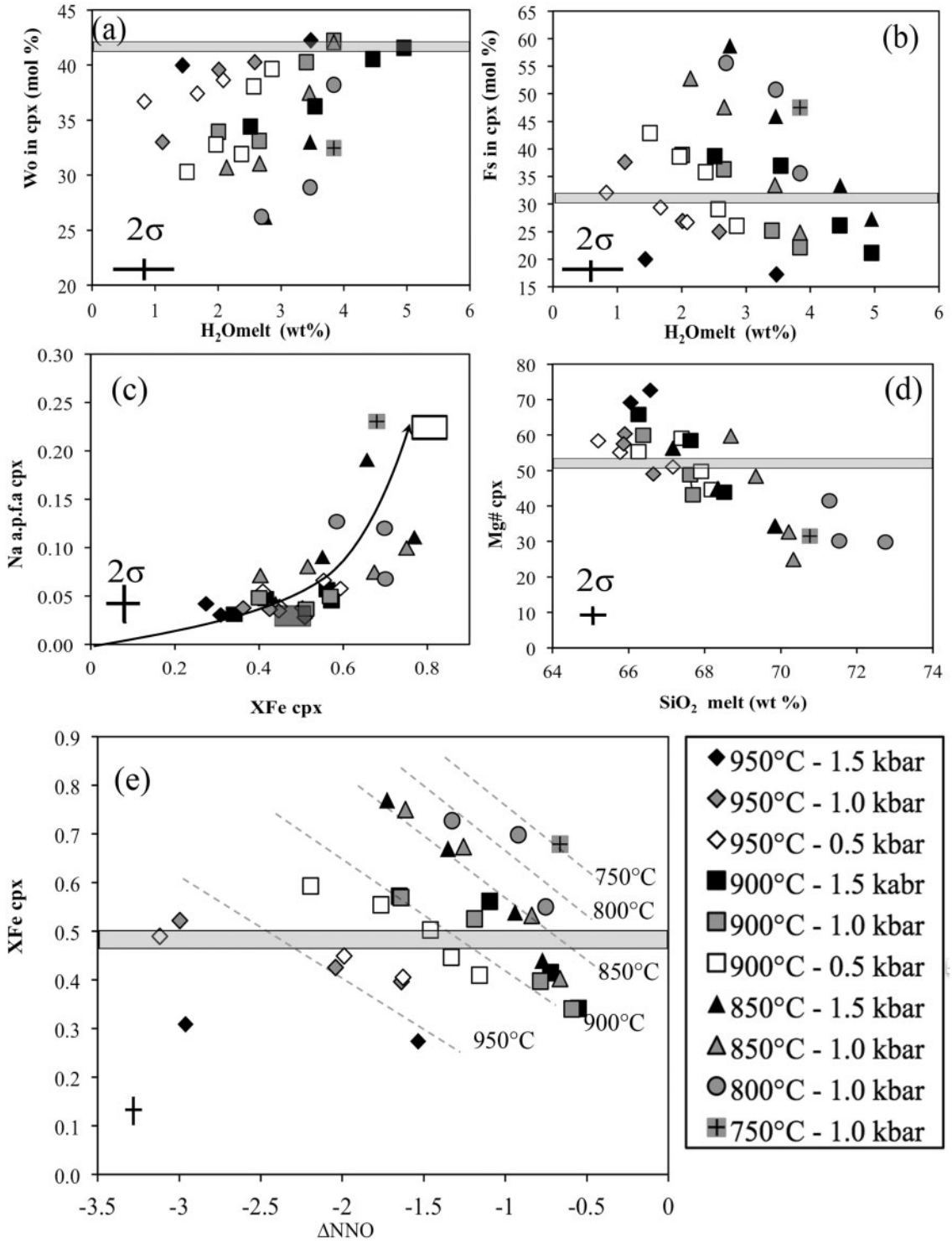

Fig. 8. Composition of experimental clinopyroxene. (a) Wo and (b) Fs contents vs mol % vs H_2O_{melt}. (c) Na vs total iron content [expressed as $X\text{Fe} = \text{Fe}_{tot}/(\text{Fe}_{tot} + \text{Mg})$], the arrow showing the direction of decreasing temperature. (d) Mg# vs SiO_2 (wt %) of coexisting melt. (e) Variation of XFe with oxygen fugacity (expressed as ΔNNO) and H_2O_{melt} in the pressure–temperature range investigated. In all panels the grey box represents the natural clinopyroxene composition; in (c) the white box indicates natural clinopyroxene compositions in pantellerites.

(Almeev *et al.*, 2012). This in large part reflects the effect of low fO_2, which promotes Fe^{2+} over Fe^{3+}, and hence stabilizes Fe-rich Ol, which, unlike Cpx, accommodates only Fe^{2+}. Considering now the hydrous phases, neither biotite (Bt) nor Amph (either calcic or sodic) has been detected in experiments or in the rocks. In contrast, Bt in dacitic (e.g. Costa *et al.*, 2004) and other more aluminous (and more iron-poor) trachytic (Martel *et al.*, 2013) melts is stable at $T < 875$°C, depending in particular on potassium content. We suggest that the lack of Bt in our

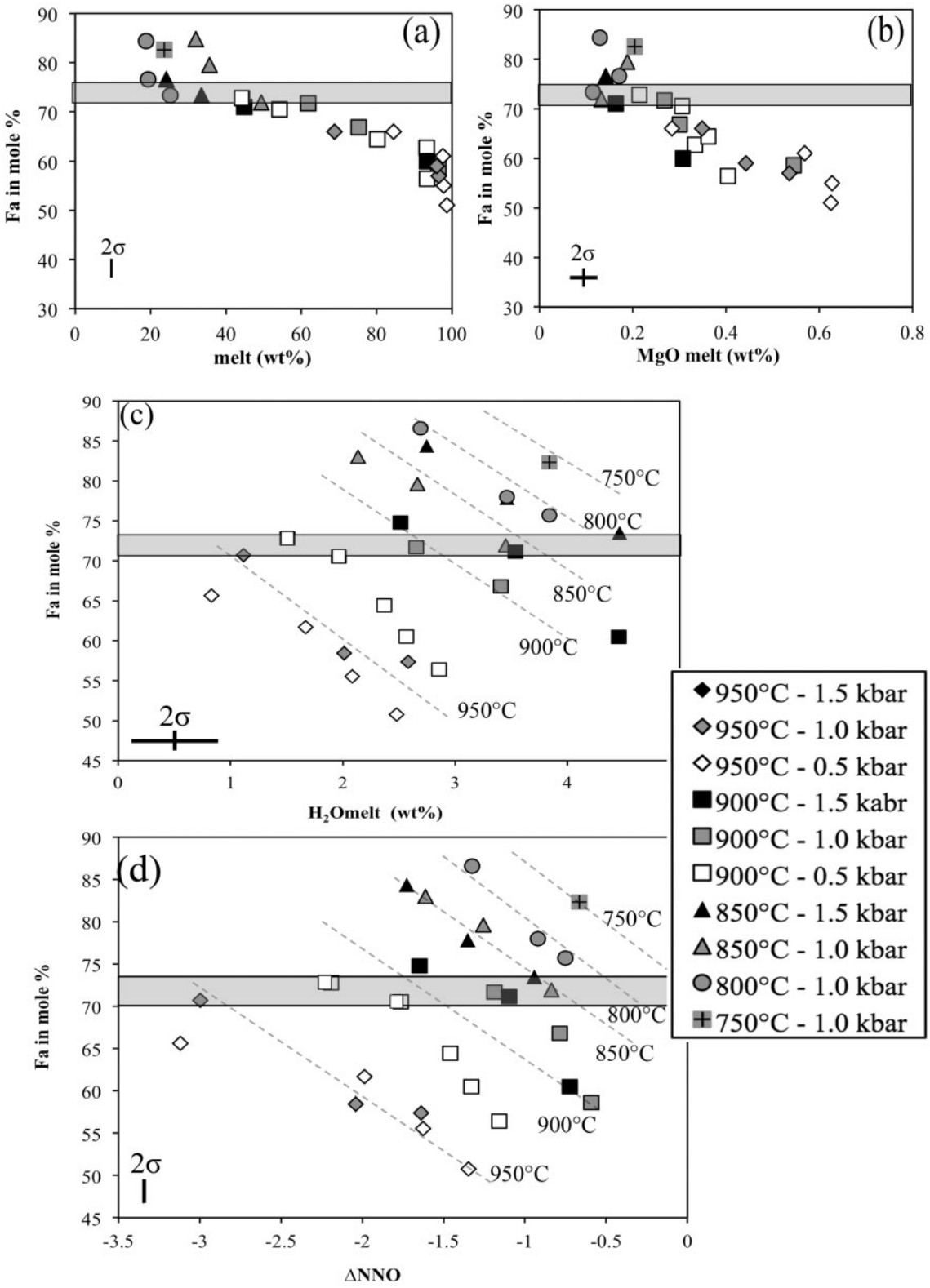

Fig. 9. Composition of experimental olivine. (a) Fa content vs melt fraction. (b) Fa vs MgO content of coexisting melt. (c) Fa content vs H_2O_{melt}. (d) Fa content vs oxygen fugacity expressed as ΔNNO.

experiments is primarily due to the peralkaline nature of the residual liquid, although Bt has been shown to crystallize in comendites, but only at very low temperatures ($<700^{\circ}$C; Scaillet & Macdonald, 2001). Regarding Amph, the relatively CaO-rich character of the bulk compositions together with the high-pressure conditions ($P \geq 2$ kbar) allow the stabilization of hornblende in dacitic magmas, as well as in the trachytes of Martel *et al.*

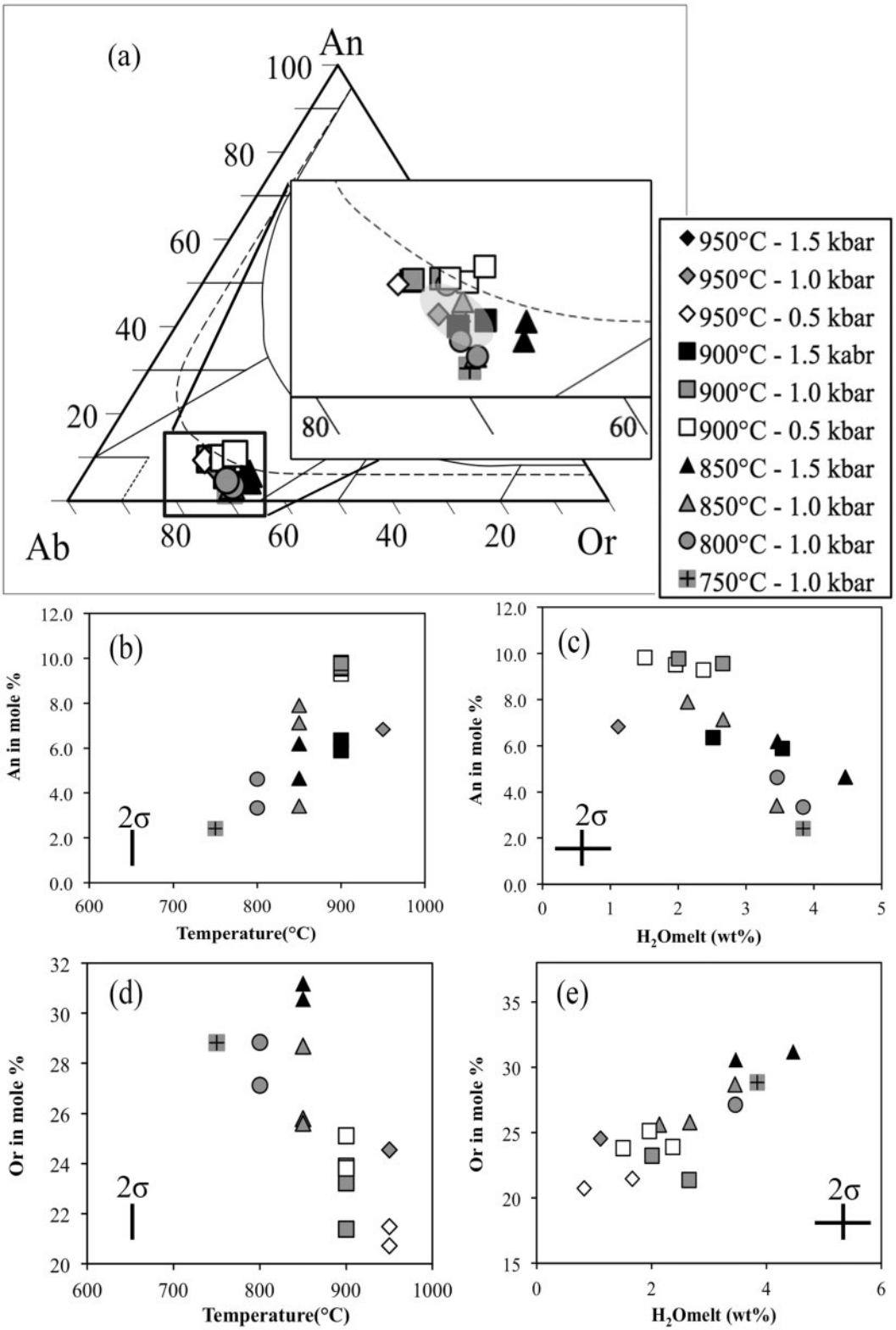

Fig. 10. (a) Composition of experimental alkali feldspar plotted in the classification diagram of Deer *et al.* (1992). All alkali feldspars plot in the field of anorthoclase. Compositional variation of experimental alkali feldspar shown with temperature and H_2O_{melt}. (b) An content (mol %) vs temperature. (c) An content vs H_2O_{melt}. (d) Or content (mol %) vs temperature. (e) Or content vs H_2O_{melt}. The grey circle indicates the composition of the natural alkali feldspar.

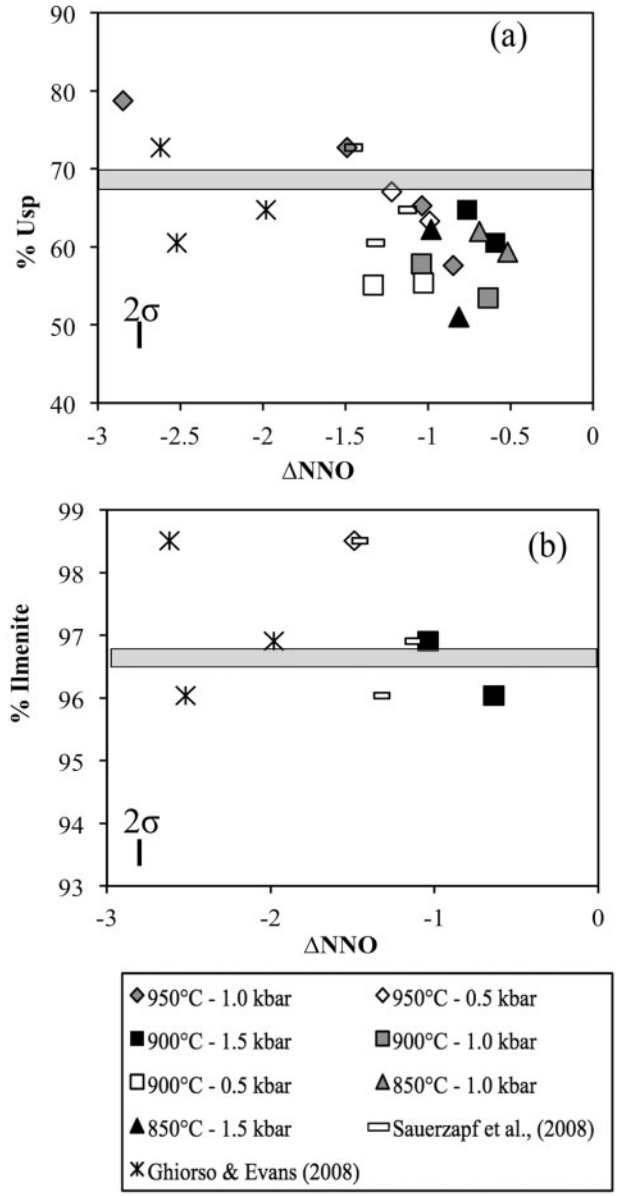

Fig. 11. Composition of experimental Fe–Ti oxides. (a) Ulvöspinel content vs oxygen fugacity expressed as ΔNNO. (b) Ilmenite content vs oxygen fugacity expressed as ΔNNO. In both projections is also plotted the oxygen fugacity calculated (see text) following the formulation of Ghiorso & Evans (2008) and Sauerzapf *et al.* (2008), for the given per cent of ulvöspinel or ilmenite components. The grey band corresponds to the composition of the natural Fe–Ti oxides. The vertical bar is the average standard deviation of experimental oxide analyses; the horizontal bar is the maximum uncertainty on oxygen fugacity.

(2013). In the latter, however, Ca-amphibole crystallized only in trachytes with at least 2 wt % CaO. The low-pressure conditions ($P \leq 1{\cdot}5$ kbar) investigated in this study are more favourable for the crystallization of Cpx, which in dacitic magmas replaces Amph at low pressure (Scaillet *et al.*, 2016). The above comparison shows how small differences in major element contents such as CaO and FeO, along with different redox conditions, influence the stability of the main mineral phases (i.e. those used to infer pre-eruption conditions) characterizing intermediate–silicic magmas. These subtle changes are not yet fully captured by existing thermodynamic models of the phase equilibria of magmas (e.g. Gualda *et al.*, 2012) which makes it all the more necessary to establish phase equilibria on a case-by-case basis (see also Cadoux *et al.*, 2014), particularly whenever pre-eruptive conditions are inferred.

Pre-eruption conditions of trachytic magmas at Pantelleria

We now turn to the pre-eruptive crystallization conditions of trachytic magmas at Pantelleria, combining the results of phase equilibrium experiments with petrological data. We mostly consider GTT, owing to its more systematic P–T–H_2O_{melt} coverage, but we note that the mineral assemblage of both samples is well reproduced in the P–T–H_2O_{melt}–fO_2 range investigated. The large coexistence field of Cpx, Ol and Af requires considerations other than phase equilibria alone to identify more precisely at which conditions phase proportions and chemical compositions similar to those observed in natural rocks can be reproduced. As mentioned above, White *et al.* (2009) obtained temperatures of 858–922°C at an fO_2 close to FMQ for the metaluminous trachytes. In detail, for the Green Tuff trachytic member they found a temperature of 904°C and fO_2 around FMQ – 1. Only the charges at 900–950°C with H_2O_{melt} between 1·5 and 3·5 wt % have crystal contents comparable with that of the natural rock (Fig. 13). Run products at $T \geq 900$°C or $T \leq 850$°C with higher H_2O_{melt} have crystal contents either too low ($T \geq 900$°C) or too high ($T \leq 850$°C) to match that of the natural rock. This is due to Af behaviour, which at $T \geq 900$°C crystallizes at H_2O_{melt}-poor conditions (i.e. $H_2O_{melt} \leq 3$ wt %), whereas at $T \leq 850$°C it joins the crystallization sequence near H_2O-saturation (Fig. 5a and b), causing a large increase in crystal content (Fig. 3a).

Additional constraints on pre-eruptive conditions are provided by mineral chemistry. Cpx and Ol compositionally similar to that of the natural trachytes were reproduced in the temperature range 850–950°C, over a fairly wide range of H_2O_{melt} (1–3 wt %). If we consider a pressure of 1 kbar, a temperature of 900°C and an oxygen fugacity of NNO – 1·3, as already inferred for the trachyte (this study; White *et al.*, 2009), using equations (1) and (2) with the composition of natural Cpx and Ol (XFe = 0·5, $Fa_{70–72}$) gives $H_2O_{melt} = 2{\cdot}3 \pm 0{\cdot}2$ wt %. Under these T–H_2O_{melt} conditions, Af is stable and its composition falls within the compositional range of the less evolved alkali feldspars typical of the natural trachyte phenocrysts. Using such a H_2O_{melt} and $T = 900$°C as inputs for equation (3) yields an anorthite content of $An_{8–10}$ for Af (i.e. similar to that of the natural phenocrysts). Similarly, at $T = 900–950$°C, experimental Fe–Ti oxides have a composition similar to those of the natural rock (Fig. 11). The lack of melt inclusion data for trachytes prevents comparison with the H_2O_{melt} inferred

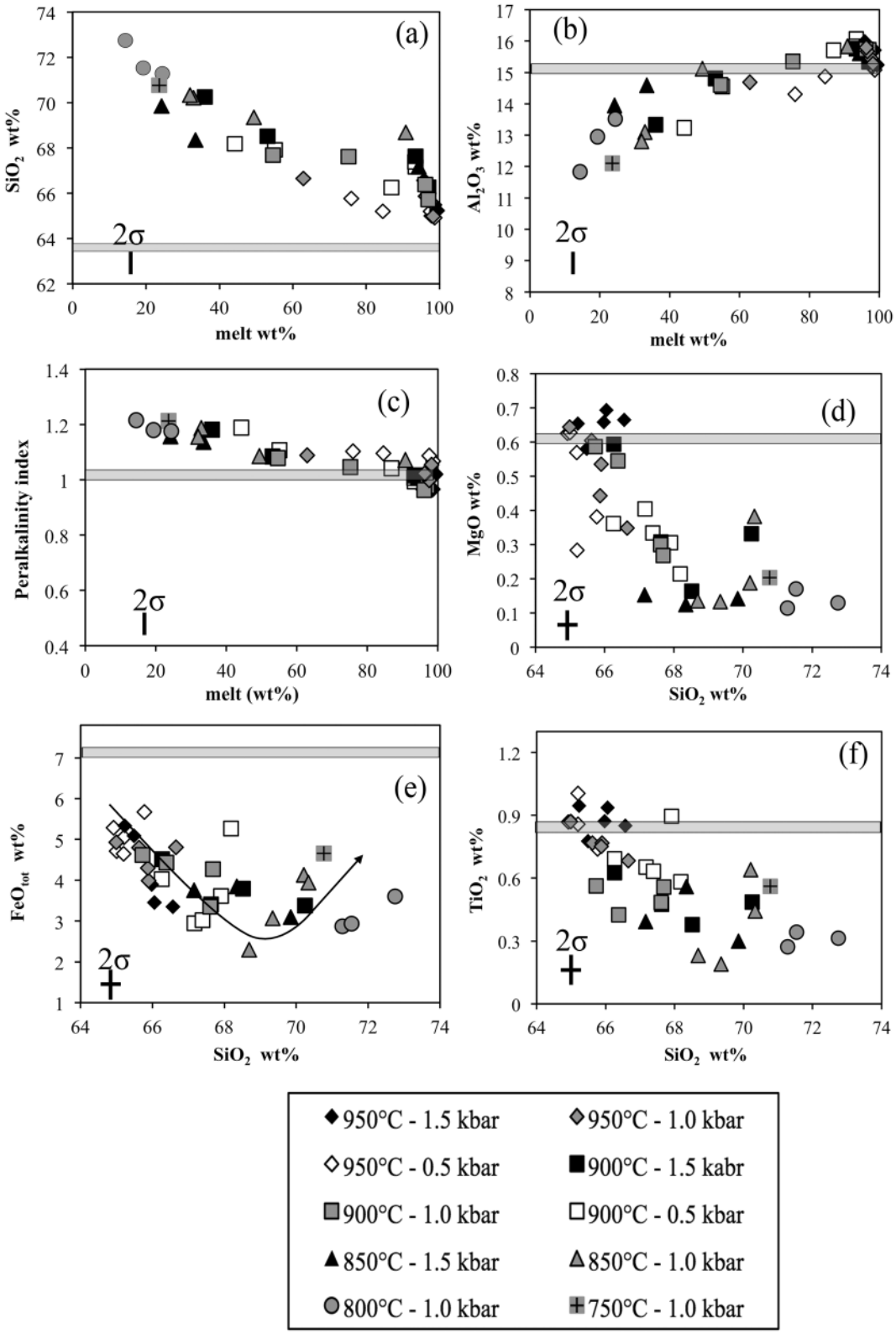

Fig. 12. Glass compositions. (a–e) Variation of major and minor oxides of experimental glasses vs either melt fraction (a–c) or SiO_2 (d–f). The grey boxes indicate the composition of the natural Green Tuff Trachyte.

from our experimental study, yet the phase relationships, crystal content and compositions suggest a maximum of 3·5 wt % H_2O_{melt}. Such an estimate of H_2O_{melt} is broadly comparable with the value (~4 wt %) inferred from MELTS calculations by White *et al.* (2009). According to those researchers, metaluminous trachytes are produced after 64% fractional crystallization of a parental basalt with a bulk H_2O_{melt} of 1·0–1·5 wt %.

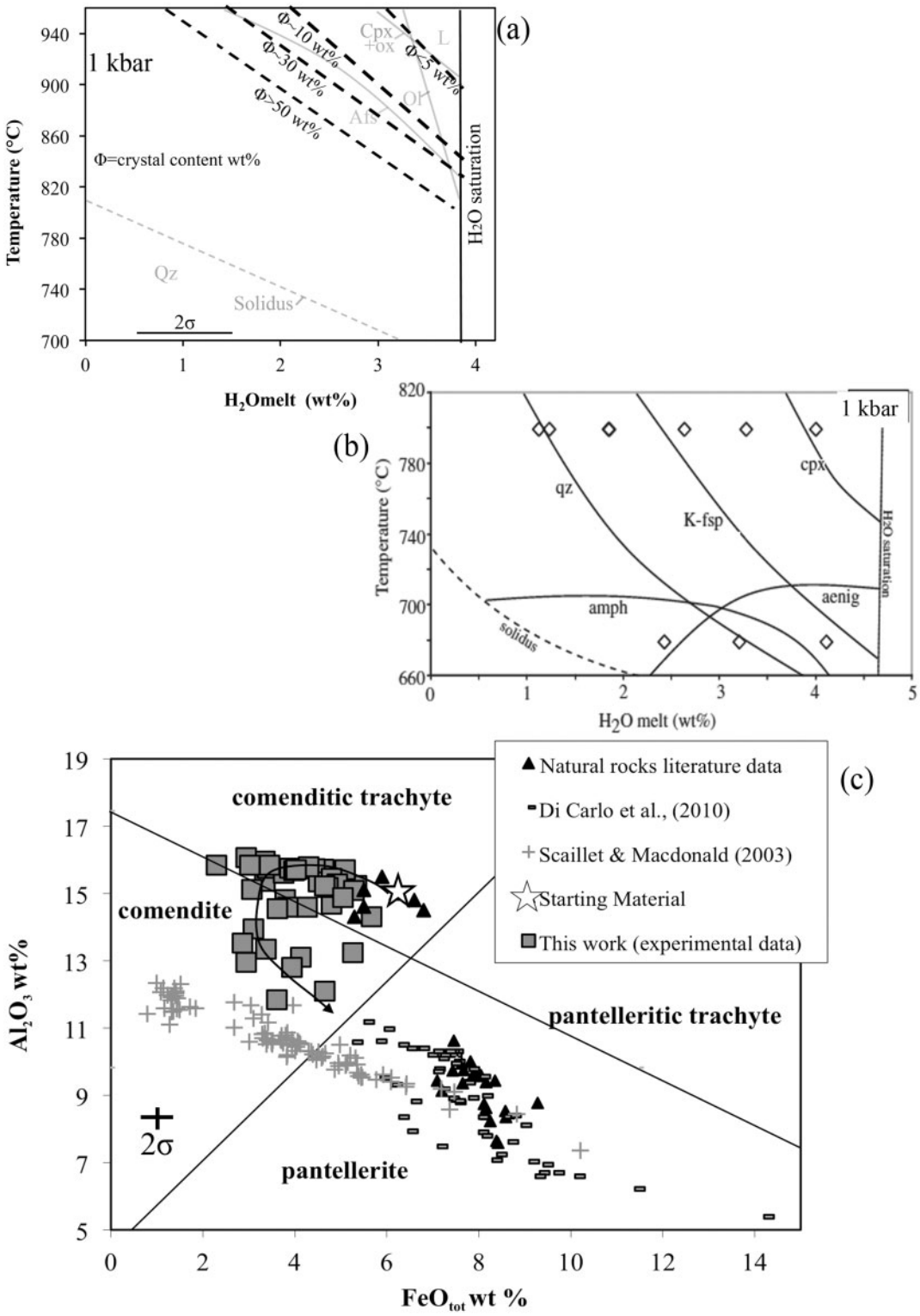

Fig. 13. (a) Phase relationships at 1 kbar of the Green Tuff trachytic member with superimposed contours (dashed lines) of crystal content (Φ, wt %). (b) Phase diagram of Pantelleria peralkaline rhyolites from Di Carlo *et al.* (2010) for comparison with the phase relationships of the Green Tuff trachytic member (a). (c) Macdonald (1974) diagram [FeO_{tot} vs Al_2O_3 (wt %)] for peralkaline rocks in which are reported the experimental results of this study and, for comparison, the experiments of Scaillet & Macdonald (2003), Di Carlo *et al.* (2010) as well as literature data taken from Civetta *et al.* (1998), Ferla & Meli (2006), Rotolo *et al.* (2007) and White *et al.* (2009).

As regards the storage pressure, at 950°C, co-crystallization of Cpx–Ol–Af is not possible above 1·5 kbar when $H_2O_{melt} = 2·2$ wt % (Fig. 6a). At 900°C, this assemblage is stable at 1·5 kbar with similar H_2O_{melt} (Fig. 6b). The pressure inferred from melt inclusions trapped in phenocrysts of the GT pantelleritic basal member (i.e. first ejected) is 0·5–0·6 kbar (Lanzo *et al.*, 2013), providing a lower pressure bound. Our results corroborate geophysical constraints, which suggest the existence of a magma reservoir at a depth of about 4 km below Pantelleria. Considering an average crustal density of 2·6 g cm^{-3}, such a depth corresponds to a lithostatic pressure of between 1 and 1·5 kbar (Mattia *et al.*, 2007).

To summarize, experimental, petrological (this study; White *et al.*, 2009), and geophysical (Mattia *et al.*, 2007) data constrain the pre-eruptive P–T–H_2O_{melt}–fO_2 conditions of Pantelleria trachytic magmas at 0·5–1·5 kbar, 925 ± 25°C, 1–3 wt % H_2O_{melt}, and NNO – 0·5 to NNO – 2.

Relation between trachytes and pantellerites

A central issue in the study of magmatism at Pantelleria, as well as in other peralkaline centers, is the origin of the more differentiated rocks (i.e. pantellerites and comendites). As already noted in the Introduction, crystal fractionation and partial melting or a combination of the two processes has been invoked to explain the genesis of pantellerite (Macdonald *et al.*, 1987; Mungall & Martin, 1995; Scaillet & Macdonald, 2003). On the basis of major and trace element modelling, most of the recent studies on Pantelleria magmatism (Civetta *et al.*, 1998; White *et al.*, 2009; Neave *et al.*, 2012), have argued for a fractional crystallization process to produce pantelleritic melts from a metaluminous parental trachyte, although Avanzinelli *et al.* (2004) proposed an origin by partial melting of gabbroid cumulates.

Civetta *et al.* (1998), using mass-balance calculations, proposed that pantelleritic melts are produced by 77–82% crystallization of a comenditic trachytic magma, with a mineral assemblage dominated by Af and subordinate aenigmatite (Aegn), Ol, Cpx or Amph and Ap. Similarly, by combining mass-balance calculations and thermodynamic modelling, White *et al.* (2009) proposed that pantellerites are produced by 80–85% crystallization of a metaluminous trachyte in the temperature interval 700–940°C, with a mineral assemblage dominated by Af, Cpx, Fe–Ti oxides and Ap. Neave *et al.* (2012) proposed a liquid line of descent from trachyte to pantellerite through a principal component analysis of natural glasses (i.e. melt inclusions and matrix glasses) and whole-rock data. They too come to the conclusion that pantellerites form via the removal of 89 wt % Af (Or_{38}), 5 wt % Cpx ($En_4Fs_{45}Wo_{35}Ae_{16}$), 6 wt % Aegn and 0·2 wt % Ilm from a parental trachytic magma.

In our study, phases controlling the trends of glass major elements are Cpx, Ol, Fe–Ti oxides and Af, as also inferred from the above-mentioned geochemical modelling, which in some cases includes Aegn, Amph and Ap. If we first consider phase proportions, a decrease in temperature from 950 to 750°C at 1 kbar increases the crystal content to 85 wt %, Af being the dominant phase (25–80 wt % of the solids), whereas the amount of Ol, Cpx and oxides remains lower than 15 wt % (Fig. 3b). These results are consistent with the phenocrysts of the natural trachytes and pantellerites, as well as with the geochemical constraints. Moreover, the results of Di Carlo *et al.* (2010) show that pantelleritic melts crystallize Af at near-liquidus conditions, which is consistent with their extraction from a parental melt saturated in Af.

Considering now the composition of the minerals from the experiments, with decreasing temperature and fO_2 Cpx has XFe > 0·75 approaching that of the Cpx in natural pantellerite (XFe > 0·80), showing also general Na_2O enrichment (Fig. 8c). The near-liquidus (at 800°C, NNO – 1·87) Cpx of Di Carlo *et al.* (2010) has an XFe = 0·82, which is close to that produced after extensive trachyte crystallization in our experiments. Similarly, the Ol crystallizing at 750°C in trachyte has a fayalite content ($Fa_{83–89}$) close to that of pantelleritic Ol (Fa_{90}). Finally, Af also shows an evolutionary trend from anorthoclase to alkali feldspar, the latter having an anorthite content lower than 2 mol % (i.e. similar to that of pantelleritic Af). Altogether, our results reproduce the observed mineralogical attributes of pantellerites, and are also in very good agreement with those of Di Carlo *et al.* (2010), in which the mineral compositions of pantelleritic rocks have been reproduced at temperatures ≤750°C and redox conditions at, or below, the FMQ buffer, supporting a genetic link between trachytes and pantellerites.

As stressed above, the crystallizing experimental phases influence the residual glass composition. In particular, the crystallization of mafic phases leads first to a decrease of melt iron content along with an increase in Al_2O_3 with respect to the starting material, lying mostly within the comenditic trachyte field in the projection scheme of Macdonald (1974) (Fig. 13c). As a consequence, experimental glasses produced at T > 850°C have FeO_{tot} contents that are below that of the starting material (Fig. 12), progressively decreasing with differentiation until a minimum of *c.* 3 wt % is achieved at 69 wt % SiO_2. This results from the predominance of mafic phases in the crystallizing assemblage, in particular Cpx. A further decrease in temperature produces the onset of massive feldspar crystallization, which rapidly becomes the dominant mineral phase (Figs 3 and 4, Table 2). This in turn results in an increase of the FeO of the residual melt, which becomes comenditic, trending toward the pantelleritic field where Pantelleria rhyolites plot (Fig. 13c).

Production of liquids more enriched in iron (and more peralkaline) can be achieved either by a slight decrease in fO_2 during the evolution of trachyte and/or by further feldspar crystallization. The first mechanism will suppress magnetite from the crystallizing assemblage,

hence leading to more FeO-rich melts. Reduction during trachyte crystallization is supported by our phase-equilibrium results, because for trachytes our data suggest redox conditions akin to magnetite crystallization (NNO – 0·5 to NNO – 1·5), whereas in pantellerites, redox conditions are too low (<NNO – 1·5) for this oxide to be stable, as observed in many strongly peralkaline rhyolites (Nicholls & Carmichael 1969). The second mechanism (i.e. feldspar crystallization) will produce an FeO increase as well, but also a decrease in Al_2O_3. As a result, the peralkalinity index of the residual liquid progressively increases as crystallization proceeds (from 0·98 to 1·21 in our experiments; Fig. 12c, Table 7). We stress that the comendite to pantellerite transition has been already experimentally demonstrated by Scaillet & Macdonald (2003): their experiments (Fig. 13c) show that pantelleritic melt production requires 40–65 wt % crystallization of comenditic magmas, depending of their maficity.

Our results thus demonstrate unambiguously, and for the first time, that peralkaline felsic derivatives can be produced from a metaluminous, more mafic, parental magma crystallizing at low pressure. The fact that both trachytic and pantelleritic magmas record similar pressures of magma storage is additional evidence of their parent–daughter relationship. In terms of volatile content, it is worth noting that both trachytic and pantelleritic magmas have significant amounts of dissolved water, the estimated H_2O_{melt} for trachytes being slightly lower than that of pantellerites. This reinforces a genetic link between the two magmas, but also presumably reflects the shallow conditions of magma storage, which constrain low water contents in the melt close to water saturation conditions. The protracted fractional crystallization needed for the trachyte–pantellerite transition, shallow storage conditions and the volatile-rich character of the parental magmas suggest that significant outgassing may take place during magma evolution at Pantelleria.

CONCLUSIONS

Our experiments on trachytes from Pantelleria extend and complement our previous experimental study on peralkaline rhyolites from the same area (Di Carlo *et al.*, 2010). Phase equilibrium experiments on trachytic samples (Green Tuff and Post Cinque Denti Caldera eruptions) have allowed us to constrain the pre-eruptive conditions of trachytic magmas at Pantelleria, whose composition bridges the compositional gap between basalts and pantellerites. The constrained conditions of magma storage, in particular pressure, are similar to those inferred for pantellerites, except for the higher temperature that reflects the maficity of the magmas. This shows that fractionation leading to peralkaline felsic derivatives is a process that occurs at shallow crustal level (e.g. Mahood, 1984). To the best of our knowledge, this is the first time that the transition between a metaluminous magma and a peralkaline derivative has been experimentally achieved at low pressure, confirming previous suggestions regarding the origin of peralkaline rhyolites by low-pressure fractional crystallization of a metaluminous, more mafic, parental magma (i.e. Civetta *et al.*, 1998), although we do not rule out other mechanisms.

ACKNOWLEDGEMENTS

This paper is part of the PhD thesis of the first author, who is deeply grateful for all the support received from the 'Magma Team' of ISTO during the long experimental work. The authors wish to thank R. Macdonald and M. Brenna for their thorough and extremely constructive reviews, which significantly improved the original paper.

REFERENCES

Albarède, F. (1995). *Introduction to Geochemical Modelling*. Cambridge Univeristy Press, 543 pp.

Almeev, R. R., Bolte, T., Nash, B. P., Holtz, F., Erdmann, M. & Cathey, H. (2012). High-temperature, low-H_2O silicic magmas of the Yellowstone Hotspot: an experimental study of rhyolite from the Bruneau–Jarbidge eruptive center, central Snake River Plain, USA. *Journal of Petrology* **53**, 1837–1866.

Andújar, J., Scaillet, B., Pichavant, M. & Druitt, T. H. (2015). Differentiation conditions of a basaltic magma from Santorini, and its bearing on the production of andesite in arc settings. *Journal of Petrology* **56**, 765–794.

Avanzinelli, R., Bindi, L., Menchetti, S. & Conticelli, S. (2004). Crystallization and genesis of peralkaline magmas from Pantelleria Volcano, Italy: an integrated petrological and crystal-chemical study. *Lithos* **73**, 41–69.

Bailey, D. K. & Macdonald, R. (1975). Fluorine and chlorine in peralkaline liquids and the need for magma generation in an open system. *Mineralogical Magazine* **40**, 405–414.

Bailey, D. K. & Macdonald, R. (1987). Dry peralkaline felsic liquids and carbon dioxide flux throught the Kenya rift zone. In: Mysen, B. (ed.) *Magmatic Processes: Physicochemical Principles. Geochemical Society*, Special Publication **1**, 91–105.

Barberi, F., Santacroce, R., Ferrara, G., Treuil, M. & Varet, J. (1975). A transitional basalt–pantellerite sequence of fractional crystallisation, the Boina centre (Afar Rift, Ethiopia). *Journal of Petrology* **16**, 22–56.

Barclay, J. & Carmichael, I. S. E. (2004). A hornblende basalt from western Mexico: water-saturated phase relations constrain a pressure–temperature window of eruptibility. *Journal of Petrology* **45**, 485–506.

Bohrson, W. A. & Reid, M. R. (1997). Genesis of silicic peralkaline volcanic rocks in an ocean island setting by crustal melting and open-system processes: Socorro Island, Mexico. *Journal of Petrology* **12**, 2405–2431.

Brenna, M., Nakada, S., Miura, D., Toshida, K., Ito, H., Hokanishi, N. & Nakai, S. (2015). A trachyte–syenite core within a basaltic nest: filtering of primitive injections by a multi-stage magma plumbing system (Oki-Dōzen, south-west Japan). *Contributions to Mineralogy and Petrology* **170**, 1–21.

Burnham, C. W., Holloway, J. R. & Davis, N. F. (1969). *Thermodynamic Properties of Water to 1000°C and 1000 bars. Geological Society of America, Special Papers* **132**, 96 pp.

Cadoux, A., Scaillet, B., Druitt, T. H. & Deloule, E. (2014). Magma storage conditions of large Plinian eruptions of Santorini. *Journal of Petrology* **55**, 1129–1171.

Caricchi, L. & Blundy, J. (2015). Experimental petrology of monotonous intermediate magmas. In: Caricchi, L. & Blundy, J. D. (eds) *Chemical, Physical and Temporal Evolution of Magmatic Systems. Geological Society, London, Special Publications* **422**.

Catalano, S., De Guidi, G., Lanzafame, G., Monaco, C. & Tortorici, L. (2009). Late Quaternary deformation on the island on Pantelleria: new constraints for the recent tectonic evolution of the Sicily Channel Rift (southern Italy). *Journal of Geodynamics* **48**, 75–82.

Chou, I.-M. (1978). Calibration of oxygen buffers at elevated *P* and *T* using the hydrogen fugacity sensor. *American Mineralogist* **63**, 690–703.

Civetta, L., Cornette, Y., Gillot, P. Y. & Orsi, G. (1988). The eruptive history of Pantelleria (Sicily Channel) in the last 50 ka. *Bulletin of Volcanology* **50**, 47–57.

Civetta, L., D'Antonio, M., Orsi, G. & Tilton, G. R. (1998). The geochemistry of volcanic rocks from Pantelleria, Sicily Channel: petrogenesis and characteristics of the mantle source region. *Journal of Petrology* **39**, 1453–1491.

Clemens, J. D. & Wall, V. J. (1981). Origin and crystallization of some peraluminous (S-type) granitic magmas. *Canadian Mineralogist* **19**, 111–131.

Costa, F., Scaillet, B. & Pichavant, M. (2004). Petrological and experimental constraints on the pre-eruptive conditions of Holocene dacite from Volcan San Pedro (36°S, Chilean Andes) and the importance of sulphur in silicic subduction-related magmas. *Journal of Petrology* **45**, 855–881.

Deer, W. A., Howie, R., A. & Zussman, J. (1992). *An Introduction to the Rock-Forming Minerals*, 2nd edn. Longman, 696 pp.

Di Carlo, I., Pichavant, M., Rotolo, S. G. & Scaillet, B. (2006). Experimental crystallization of a high-K arc basalt: the golden pumice, Stromboli volcano (Italy). *Journal of Petrology* **47**, 1317–1343.

Di Carlo, I., Rotolo, S. G., Scaillet, B., Buccheri, V. & Pichavant, M. (2010). Phase equilibrium constraints on pre-eruptive conditions of recent felsic explosive volcanism at Pantelleria Island, Italy. *Journal of Petrology* **51**, 2245–2276.

Ferla, P. & Meli, C. (2006). Evidence of magma mixing in the 'Daly gap' of alkaline suites: a case study from the enclave of Pantelleria (Italy). *Journal of Petrology* **47**, 1467–1507.

Ghiorso, M. S. & Evans, B. W. (2008). Thermodynamics of rhombohedral oxide solid solutions and a revision of the Fe–Ti two-oxide geothermometer and oxygen-barometer. *American Journal of Science* **308**, 957–1039.

Gioncada, A. & Landi, P. (2010). The pre-eruptive volatile contents of recent basaltic and pantelleritic magmas at Pantelleria (Italy). *Journal of Volcanology and Geothermal Research* **189**, 191–201.

Green, D. H. & Ringwood, A. E. (1967). The genesis of basaltic magmas. *Contributions to Mineralogy and Petrology* **15**, 103–109.

Gualda, G. A., Ghiorso, M. S., Lemons, R. V. & Carley, T. L. (2012). Rhyolite-MELTS: a modified calibration of MELTS optimized for silica-rich, fluid-bearing magmatic systems. *Journal of Petrology* **53**, 875–890.

Hanson, B., Delano, J. W. & Lindstrom, D. J. (1996). High-precision analysis of hydrous rhyolitic glass inclusions in quartz phenocrysts using the electron microprobe and INAA. *American Mineralogist* **81**, 1249–1262.

Johnson, M. C. & Rutherford, M. J. (1989). Experimentally determined conditions in the Fish Canyon Tuff, Colorado, magma chamber. *Journal of Petrology* **30**, 711–737.

Kelly, J. T., Carey, S., Pistolesi, M., Rosi, M., Lynn Croff-Bell, K., Roman, C. & Marani, M. (2014). Exploration of the 1891 Foerstner submarine vent site (Pantelleria, Italy): insights into the formation of basaltic balloons. *Bulletin of Volcanology* **76**, 1–18.

Landi, P. & Rotolo, S. G. (2015). Cooling and crystallization recorded in trachytic enclaves hosted inpantelleritic magmas (Pantelleria, Italy): implications for pantellerite petrogenesis. *Journal of Volcanology and Geothermal Research* **301**, 169–179.

Lanzo, G., Landi, P. & Rotolo, S. G. (2013). Volatiles in pantellerite magmas: a case study of the Green Tuff Plinian eruption (Island of Pantelleria, Italy). *Journal of Volcanology and Geothermal Research* **262**, 153–163.

Le Bas, M. J. L., Maitre, R. W. L., Streckeisen, A. & Zanettin, B. (1986). A chemical classification of volcanic rocks based on the total alkali–silica diagram. *Journal of Petrology* **27**, 745–750.

Liu, R., Fan, Q. & Zheng, X. (1998). The magma evolution of Tianchi volcano, Changbaishan. *Science of China* **41**, 382–389.

Lowenstern, J. B. & Mahood, G. A. (1991). New data on magmatic H_2O contents of pantellerites, with implications for petrogenesis and eruptive dynamics at Pantelleria. *Bulletin of Volcanology* **54**, 78–83.

Macdonald, R. (1974). Nomenclature and petrochemistry of the peralkaline oversaturated extrusive rocks. *Bulletin Volcanologique* **38**, 498–505.

Macdonald, R., Davies, G. R., Bliss, C. M., Leat, P. T., Bailey, D. K. & Smith, R. L. (1987). Geochemistry of high-silica peralkaline rhyolites, Naivasha, Kenya rift valley. *Journal of Petrology* **28**, 979–1008.

Macdonald, R., McGarvie, D. W., Pinkerton, H., Smith, R. L. & Palacz, A. (1990). Petrogenetic evolution of the Torfajökull volcanic complex, Iceland I. Relationship between the magmas types. *Journal of Petrology* **31**, 429–459.

Mahood, G. A. (1984). Pyroclastic rocks and calderas associated with strongly peralkaline magmatism. *Journal of Geophysical Research* **89**, 8540–8552.

Mahood, G. A. & Hildreth, W. (1986). Geology of the peralkaline volcano at Pantelleria, Strait of Sicily. *Bulletin of Volcanology* **48**, 143–172.

Martel, C., Pichavant, M., Holtz, F., Scaillet, B., Bourdier, J.-L. & Traineau, H. (1999). Effects of fO_2 and H_2O on andesitic phase-relationships between 2 and 4 kbar. *Journal of Geophysical Research* **104**, 29453–29470.

Martel, C., Champallier, R., Prouteau, G., Pichavant, P., Arbaret, L., Balcone-Boissard, H., Boudon, G., Boivin, P., Bourdier, J.-L. & Scaillet, B. (2013). Trachyte phase relations and implication for magma storage conditions in the Chaîne des Puys (French Massif Central). *Journal of Petrology* **54**, 1071–1107.

Mattia, M., Bonaccorso, A. & Guglielmino, F. (2007). Ground deformations in the island of Pantelleria (Italy): insights into the dynamic of the current intereruptive period. *Journal of Geophysical Research* **112**.

McMillan, P. F. & Wolf, G. H. (1995). Vibrational spectroscopy of silicate liquids. In: Stebbins, J. F., McMillan, P. F. & Dingwell, D. B. (eds) *Structure, Dynamics and Properties of Silicate Melts* 32, 247–316.

Morgan, G. B., VI & London, D. (1996). Optimizing the electron microprobe analysis of hydrous alkali aluminosilicate glasses. *American Mineralogist* **81**, 1176–1185.

Morgan, G. B., VI & London, D. (2005). Effect of current density on the electron microprobe analysis of alkali aluminosilicate glasses. *American Mineralogist* **90**, 1131–1138.

Morimoto, N. (1989). Nomenclature of pyroxenes. Subcommittee on pyroxenes, Commission on new minerals and mineral names. *Canadian Mineralogist* **27**, 143–156.

Mungall, J. E. & Martin, R. F. (1995). Petrogenesis of basalt–comendite and basalt–pantellerite suites, Terceira, Azores, and

some implications for the origin of ocean-island rhyolites. *Contributions to Mineralogy and Petrology* **119**, 43–55.

Mysen, B. O. (1983). The structure of silicate melts. *Annual Review of Earth and Planetary Sciences* **11**, 75–97.

Neave, D. A., Fabbro, G., Herd, R. A., Petrone, C. M. & Edmonds, M. (2012). Melting, differentiation and degassing at the Pantelleria volcano, Italy. *Journal of Petrology* **53**, 637–663.

Nicholls, J. & Carmichael, I. S. E. (1969). Peralkaline acid liquids: a petrological study. *Contributions to Mineralogy and Petrology* **20**, 268–294.

Pichavant, M. (1987). Effects of B and H_2O on liquidus phase relations in the haplogranite system at 1 kbar. *American Mineralogist* **72**, 1056–1070.

Pichavant, M., Martel, C., Bourdier, J.-J. & Scaillet, B. (2002). Physical conditions, structure and dynamics of a zoned magma chamber: Mount Pelée (Martinique, Lesser Antilles arc). *Journal of Geophysical Research* **107**.

Pichavant, M., Costa, F., Burgisser, A., Scaillet, B., Martel, C. & Poussineau, S. (2007). Equilibration scales in silicic to intermediate magmas—implication for experimental studies. *Journal of Petrology* **48**, 1955–1972.

Pownceby, M. I. & O'Neill, H. S. C. (1994). Thermodynamic data from redox reactions at high temperatures. III. Activity–composition relations in Ni–Pd alloys from EMF measurements at 850–1250 K, and calibration of the NiO–Ni–Pd assemblage as a redox sensor. *Contributions to Mineralogy and Petrology* **116**, 327–339.

Prosperini, N., Perugini, D., Poli, G. & Manetti, P. (2000). Magmatic enclaves distribution within the Khaggiar lava dome (Pantelleria, Italy): implication for magma chamber dynamics and eruption. *Acta Vulcanologica* **12**, 37–47.

Robie, R. A., Hemingway, B. S. & Fisher, J. R. (1979). *Thermodynamic properties of minerals and related substances at 298·15 K and 1 bar (105 Pascals) pressure and at higher temperature. US Geological Survey Bulletin* **1452**.

Romengo, N. (2011). Relationships between mafic and felsic magmatism at Pantelleria: a petrological study on intermediate trachyte magmas. PhD thesis, University of Palermo.

Romengo, N., Landi, P. & Rotolo, S. G. (2012). Evidence of basaltic magma intrusions in a trachytic magma chamber at Pantelleria (Italy). *Periodico di Mineralogia* **81**, 163–178.

Rotolo, S. G., Castorina, F., Cellura, D. & Pompilio, M. (2006). Petrology and geochemistry of submarine volcanism in the Sicily Channel Rift. *Journal of Geology* **114**, 355–365.

Rotolo, S. G., La Felice, S., Mangalaviti, A. & Landi, P. (2007). Geology and petrochemistry of recent (<25 ka) silicic volcanism at Pantelleria Island. *Bollettino della Società Geologica Italiana* **126**, 191–208.

Rotolo, S. G., Scaillet, S., La Felice, S. & Vita-Scaillet, G. (2013). A revision of the structure and stratigraphy of pre-Green Tuff ignimbrites at Pantelleria (Strait of Sicily). *Journal of Volcanology and Geothermal Research* **250**, 61–74.

Sauerzapf, U., Lattard, D., Burchard, M. & Engelmann, R. (2008). The titanomagnetite–ilmenite equilibrium: new experimental data and thermo-oxybarometric application to the crystallization of basic to intermediate rocks. *Journal of Petrology* **49**, 1161–1185.

Scaillet, B. & Evans, B. W. (1999). The 15 June 1991 eruption of Mount Pinatubo. I. Phase equilibria and pre-eruption P–T–fO_2–fH_2O conditions of the dacite magma. *Journal of Petrology* **40**, 381–411.

Scaillet, B. & Macdonald, R. (2001). Phase relations of peralkaline silicic magmas and petrogenetic implications. *Journal of Petrology* **42**, 825–845.

Scaillet, B. & Macdonald, R. (2003). Experimental constraints on the relationships between peralkaline rhyolites of the Kenya rift valley. *Journal of Petrology* **44**, 1867–1894.

Scaillet, B. & Macdonald, R. (2006). Experimental constraints on pre-eruption conditions of pantelleritic magmas: evidence from the Eburru complex, Kenya Rift. *Lithos* **91**, 95–108.

Scaillet, B., Pichavant, M., Roux, J., Humbert, G. & Lefèvre, A. (1992). Improvements of the Shaw membrane technique for measurement and control of fH_2 at high temperatures and pressures. *American Mineralogist* **77**, 647–655.

Scaillet, B., Pichavant, M. & Roux, J. (1995). Experimental crystallization of leucogranite magmas. *Journal of Petrology* **36**, 635–705.

Scaillet, S., Rotolo, S. G., La Felice, S. & Vita, G. (2011). High-resolution $^{40}Ar/^{39}Ar$ chronostratigraphy of the post-caldera (<20 ka) volcanic activity at Pantelleria, Sicily Strait. *Earth and Planetary Science Letters* **309**, 280–290.

Scaillet, S., Vita-Scaillet, G. & Rotolo, S. G. (2013). Millennial-scale phase relationships between ice-core and Mediterranean marine records: insights from high-precision $^{40}Ar/^{39}Ar$ dating of the Green Tuff of Pantelleria, Sicily Strait. *Quaternary Science Reviews* **78**, 141–154.

Scaillet, B., Holtz, F. & Pichavant, M. (2016). Experimental constraints on the formation of silicic magmas. *Elements* **12**, 109–114.

Selbekk, R. S. & Tronnes, R. G. (2007). The 1362 AD Oraefajokull eruption, Iceland: petrology and geochemistry of large-volume homogeneous rhyolites. *Journal of Volcanology and Geothermal. Research* **160**, 42–58.

Sisson, T. & Grove, T. L. (1993). Experimental investigations of the role of H_2O in calc-alkaline differentiation and subduction zone magmatism. *Contribution to Mineralogy and Petrology* **113**, 143–166.

Speranza, F., Landi, P., D'Ajello Caracciolo, F. & Pignatelli, A. (2012). Paleomagnetic dating of the most recent silicic eruptive activity at Pantelleria (Strait of Sicily). *Bulletin of Volcanology* **72**, 847–858.

Spray, J. G. & Rae, D. A. (1995). Quantitative electron-microprobe analysis of alkali silicate glasses: a review and user guide. *Canadian Mineralogist* **33**, 323–332.

Taylor, J. R., Wall, V. J. & Pownceby, M. I. (1992). The calibration and application of accurate redox sensors. *American Mineralogist* **77**, 284–295.

Villari, L. (1974). The island of Pantelleria. *Bulletin Volcanologique* **38**, 680–724.

White, J. C., Ren, M. & Parker, D. F. (2005). Variation in mineralogy, temperature, and oxygen fugacity in a suite of strongly peralkaline lavas and tuffs, Pantelleria, Italy. *Canadian Mineralogist* **43**, 1331–1347.

White, J. C., Parker, D. F. & Ren, M. (2009). The origin of trachyte and pantellerite from Pantelleria, Italy: insights from major element, trace element, and thermodynamic modelling. *Journal of Volcanology and Geothermal Research* **179**, 33–55.

Williams, R. (2010). Emplacement of radial pyroclastic density currents over irregular topography: the chemically zoned, low aspect-ratio Green Tuff ignimbrite. PhD thesis, University of Leicester, 232 pp.